

LUSIFER: a LUCid approach to SIX-FERMion production

STEFAN DITTMAYER^{1†} AND MARKUS ROTH²

¹ *Deutsches Elektronen-Synchrotron DESY
 D-22603 Hamburg, Germany*

² *Institut für Theoretische Physik, Universität Karlsruhe
 D-76131 Karlsruhe, Germany*

Abstract:

LUSIFER is a Monte Carlo event generator for all processes $e^+e^- \rightarrow 6$ fermions, which is based on the multi-channel Monte Carlo integration technique and employs the full set of tree-level diagrams. External fermions are taken to be massless, but can be arbitrarily polarized. The calculation of the helicity amplitudes and of the squared matrix elements is presented in a compact way. Initial-state radiation is included at the leading logarithmic level using the structure-function approach. The discussion of numerical results contains a comprehensive list of cross sections relevant for a 500 GeV collider, including a tuned comparison to results obtained with the combination of the WHIZARD and MADGRAPH packages as far as possible. Moreover, for off-shell top-quark pair production and the production of a Higgs boson in the intermediate mass range we additionally discuss some phenomenologically interesting distributions. Finally, we numerically analyze the effects of gauge-invariance violation by comparing various ways of introducing decay widths of intermediate top quarks, gauge and Higgs bosons.

June 2002

[†]Heisenberg fellow of the Deutsche Forschungsgemeinschaft

1 Introduction

At future e^+e^- colliders, such as TESLA [1], some of the most interesting elementary particle reactions lead to final states involving six fermions. Typically these multi-particle final states represent the final decay stage of unstable particles that were produced as resonances in subprocesses. Because of the high precision of future colliders, predictions that are entirely based on the narrow-width approximation (with possible improvements by spin correlations between production and decays or by resonance expansions) are not sufficient in the most cases. In practice, this means that the full set of Feynman diagrams (not only the resonant ones) has to be considered in perturbative calculations, at least in lowest order. The situation is very similar to four-fermion production, $e^+e^- \rightarrow 4f$, and the related radiative processes $e^+e^- \rightarrow 4f + \gamma$, at LEP2 [2]. Although the complexity of the corresponding calculations increases when turning from four-fermion to six-fermion production, $e^+e^- \rightarrow 6f$, most of the existing results are obtained by applying and further developing the methods that had been worked out for four-fermion production. We briefly summarize these results according to the subprocesses of interest:

(i) Top-quark pair production

Since top quarks decay via the cascade $t \rightarrow bW^+ \rightarrow bf\bar{f}'$ into three fermions, the production of $t\bar{t}$ pairs corresponds to a particular class of $e^+e^- \rightarrow 6f$ processes: $e^+e^- \rightarrow b\bar{b}f_1\bar{f}'_1f_2\bar{f}'_2$. Here $f_i\bar{f}'_i$ denote two weak isospin doublets. Some processes are already discussed in the literature. The specific process $e^+e^- \rightarrow b\bar{b}u\bar{d}\mu^-\bar{\nu}_\mu$ was studied in Ref. [3] with the GRACE package [4]. In Refs. [5, 6] and Ref. [7] the cases of one and two hadronically decaying W bosons were discussed in more detail, respectively. The former results are based on a generalization of the program PHACT [8], the latter on the ALPHA algorithm [9] for matrix elements. Recently various resonance approximations for the top quarks were compared with a calculation based on full sets of $e^+e^- \rightarrow 6f$ diagrams in Ref. [10]; these results underline the importance of calculations based on full sets of Feynman diagrams. However, to our knowledge, results have not yet been presented for all final states, for instance, not yet for $e^+e^- \rightarrow b\bar{b}e^-\bar{\nu}_e\nu_e e^+$.

(ii) Vector-boson scattering and quartic gauge-boson couplings

One of the most promising windows to electroweak symmetry breaking is provided by investigating the scattering of massive vector bosons, $V_1V_2 \rightarrow V_3V_4$. This subprocess is initiated by the emission of the vector bosons $V_{1,2}$ from the incoming e^+e^- system and leads to six fermions in the final state: two remnants from the initial state and four fermions from the decays of the vector bosons $V_{3,4}$. Thus, the corresponding reactions are of the form $e^+e^- \rightarrow e^+e^-/e^+\nu_e/\bar{\nu}_e e^-/\bar{\nu}_e\nu_e + 4f$. Many studies of vector-boson scattering were presented in the literature (see e.g. Ref. [1] and references therein), but with very few exceptions they were based on approximations with respect to the kinematics of the incoming and/or the outgoing vector bosons. In Refs. [11, 12] the sensitivity of the processes $e^+e^- \rightarrow \nu_e\bar{\nu}_e + 4$ quarks to possible anomalous quartic gauge-boson couplings was investigated making use of full $e^+e^- \rightarrow 6f$ matrix elements. The matrix elements used in Ref. [11] were obtained with ALPHA, while in Ref. [12] the package O'MEGA [13] delivered the amplitudes and the phase-space generation was performed with WHIZARD [14].

(iii) *Higgs production for intermediate Higgs-boson masses*

If the Higgs boson of the Standard Model has an intermediate mass of $M_H \gtrsim 150$ GeV, it predominantly decays via $H \rightarrow WW \rightarrow 4f$. Since the Higgs boson is either produced by Higgs-strahlung off Z bosons, $e^+e^- \rightarrow ZH$, or vector-boson fusion, $e^+e^- \rightarrow e^+e^-H/\bar{\nu}_e\nu_eH$, the search for the Higgs boson in the intermediate mass range also proceeds via $e^+e^- \rightarrow 6f$ processes. In Refs. [6, 15, 16, 17] the Higgs-strahlung signal was studied for various $6f$ final states by employing full matrix elements from PHACT and ALPHA. Ref. [17] also contains some results for the vector-boson fusion channel.

(iv) *Three-gauge-boson production*

Last but not least, all $6f$ final states in $e^+e^- \rightarrow 6f$ contribute to the signal of resonant three-gauge-boson production, such as $e^+e^- \rightarrow WWZ/ZZZ$, from which valuable information on the quartic gauge-boson couplings can be deduced. In Refs. [5, 6] WWZ production was investigated for some interesting final states using the full $6f$ matrix elements from PHACT. However, more detailed studies including more final states are certainly wanted.

It should be mentioned that the combination of the PHEGAS and HELAC packages [18] is also able to deal with six-fermion production processes. However, no detailed results of these programs for $e^+e^- \rightarrow 6f$ have been presented yet in the literature.

In this paper we present the Monte Carlo event generator LUSIFER, which is, in its first version, designed for all Standard Model processes $e^+e^- \rightarrow 6$ fermions in lowest order; gluon-exchange diagrams can be optionally included for final states with two leptons and four quarks (not yet for six-quark final states).¹ Technically the approach closely follows the structure of EXCALIBUR [20] and the lowest-order part of RACOONWW [21, 22] for the processes $e^+e^- \rightarrow 4f(+\gamma)$. This means the matrix elements are evaluated within the Weyl-van der Waerden (WvdW) spinor technique as described in Ref. [23] (see also references therein); the external fermions are taken to be massless, but can be arbitrarily polarized. The phase-space integration is performed with the multi-channel Monte Carlo integration technique [24], improved by adaptive weight optimization [25]. The lowest-order predictions obtained this way are dressed by initial-state radiation (ISR) in the leading logarithmic approximation following the structure-function approach [26], as summarized in the appendix of Ref. [27].

Although the above list of topics shows that several studies of six-fermion production processes have already been presented in the literature, no detailed tuned comparison between results from different approaches is available yet. We make a first step to fill this gap by giving a full list of cross sections for $6f$ states with up to three neutrinos and up to four quarks for a centre-of-mass (CM) energy of 500 GeV. Moreover, we compare these cross sections with results obtained by WHIZARD [14] and MADGRAPH [28] as far as the combination of these packages is applicable. In general, we find good numerical agreement, but for several channels the limitation of these multi-purpose programs becomes visible. We continue the tuned comparison by comparing some distributions for topics of phenomenological interest, such as invariant-mass and angular distributions for top-

¹A full treatment of the production of four or more jets in $e^+e^- \rightarrow 6\text{jet}$ reactions additionally requires the inclusion of gluon jets, as for instance done in Ref. [19].

quark and Higgs-boson production. We conclude the discussion of numerical results by comparing various schemes for introducing the finite decay widths of unstable particles in the amplitudes. Already for CM energies in the TeV range the gauge-invariance-breaking effects in some cases are clearly visible, underlining the importance of this issue. Within LUSIFER several width schemes are implemented, comprising also the *complex-mass scheme*, which was introduced in Ref. [21] for tree-level predictions and maintains gauge invariance. Hence, gauge-violating artefacts can be controlled by comparing a given width scheme with the complex-mass scheme.

The paper is organized as follows: In Section 2 the calculation of the helicity amplitudes and of the squared matrix elements is described in detail, followed by a description of the multi-channel phase-space integration in Section 3. The treatment of ISR is described in Section 4. Section 5 contains a classification of the processes $e^+e^- \rightarrow 6f$ according to the underlying resonance subprocesses. In Section 6 we present numerical results, including a comprehensive list of cross sections, their tuned comparison with WHIZARD and MADGRAPH results, some distributions relevant for top-quark and Higgs-boson production, and the discussion of gauge-invariance-breaking effects. A summary is given in Section 7.

2 Matrix-element calculation

2.1 Generic amplitudes for eight external fermions

The Feynman diagrams contributing to a process with 8 external fermions can be classified into different categories according to the number of external fermion–antifermion pairs that directly fuse to a boson. At tree level there are at least two such pairs, called “fermion currents” in the following, so that we have three categories: diagrams with 4, 3, or 2 fermion currents. Assuming massless external fermions, the generic diagrams of these classes are shown in Figures 1–3. The vector bosons V_{\dots} represent all gauge-boson fields γ , Z , W^{\pm} , g that are allowed by the quantum numbers of the external fermions. Whenever a gauge boson has to be electrically charged, it is already denoted by W ; if a top quark is present, the charge flow is automatically fixed in the diagram. All purely electroweak diagrams are supported for arbitrary six-fermion final states. LUSIFER optionally includes also gluon-exchange diagrams, but in its first version such diagrams are only included for up to four quarks in the final state. This, in particular, implies that there are no gluonic diagrams of the type shown in Figure 1. The scalar boson S stands both for the Higgs-boson field H and for the would-be Goldstone partners χ and ϕ^{\pm} of the gauge bosons Z and W^{\pm} . The amplitudes given below are all evaluated within the ‘t Hooft–Feynman gauge. Among the internal fermions F_{\dots} the top quark plays a special role, since it is the only fermion that receives a mass, m_t . Note that the first three diagrams in each class appear already in a theory with only massless fermions, while diagrams (3d), (3e), and (2d) are proportional to a power of the top-quark mass due to the appearance of the top-quark Yukawa coupling in the amplitude.

In the generic diagrams the external fermions $f_{a,\dots,h}$, which are simply denoted as a, \dots, h , carry incoming momenta $p_{a,\dots,h}$ and helicities $\sigma_{a,\dots,h}$, respectively. The helicity amplitudes of these diagrams are calculated within the Weyl–van der Waerden (WvdW)

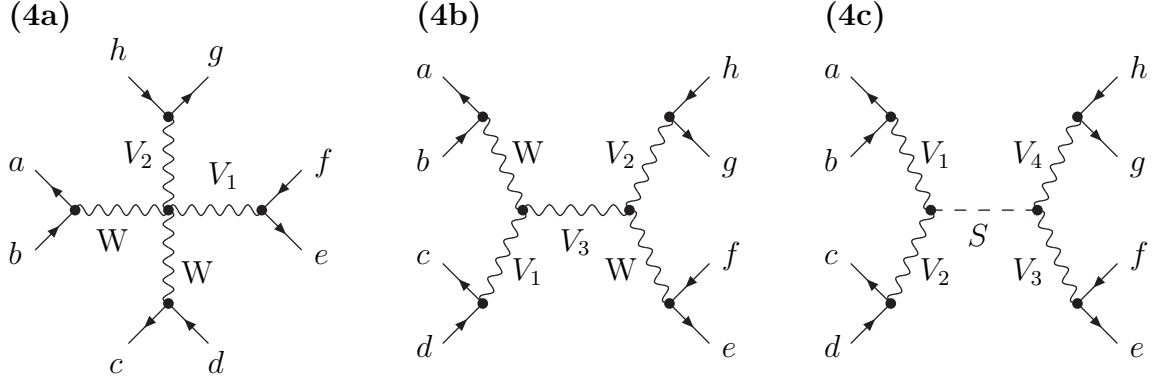


Figure 1: Generic diagrams with 4 fermion currents

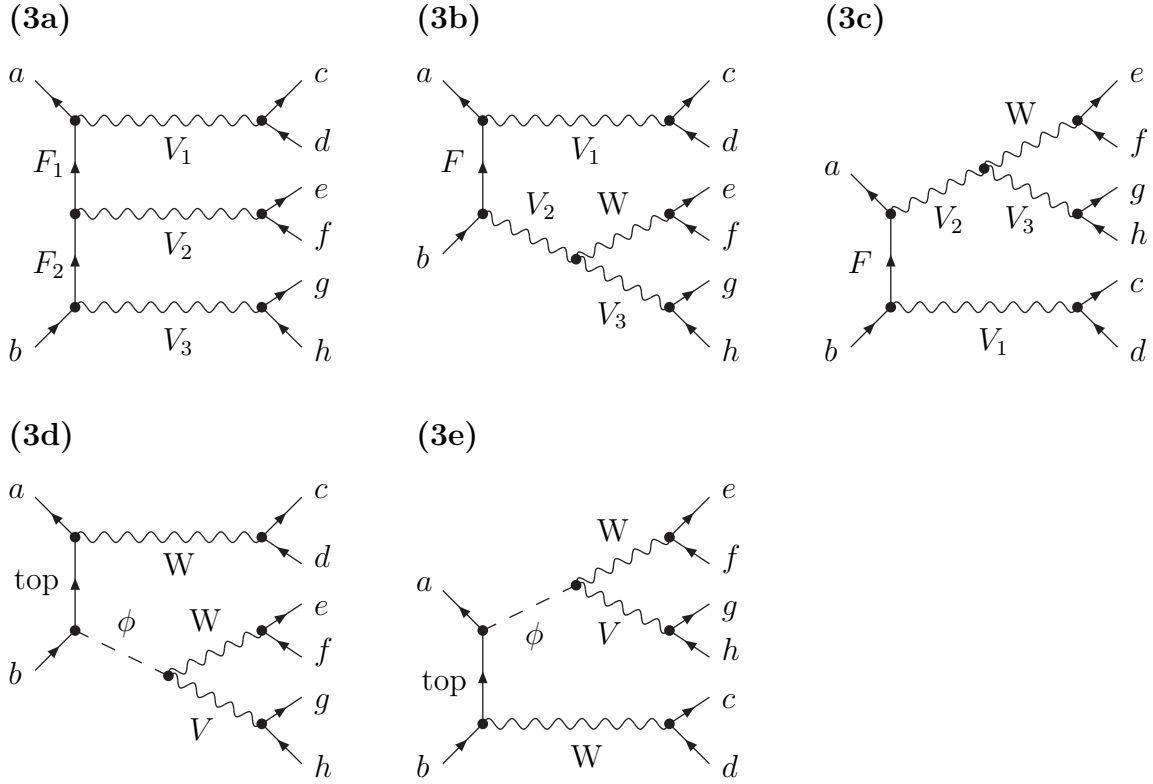


Figure 2: Generic diagrams with 3 fermion currents

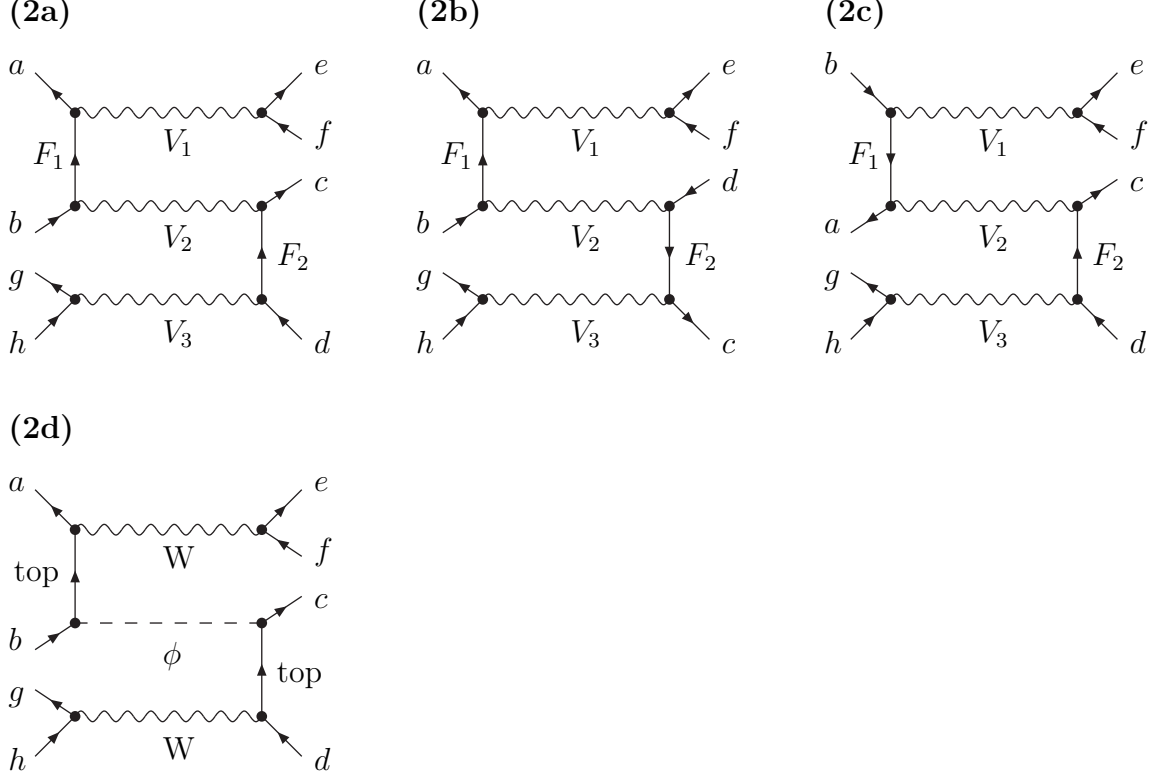


Figure 3: Generic diagrams with 2 fermion currents

formalism following the conventions of Ref. [23]. The amplitudes are expressed in terms of WvdW spinor products,

$$\langle pq \rangle = \epsilon^{AB} p_A q_B = 2\sqrt{p_0 q_0} \left[e^{-i\phi_p} \cos \frac{\theta_p}{2} \sin \frac{\theta_q}{2} - e^{-i\phi_q} \cos \frac{\theta_q}{2} \sin \frac{\theta_p}{2} \right], \quad (2.1)$$

where p_A, q_A are the associated momentum spinors for the massless momenta

$$\begin{aligned} p^\mu &= p_0(1, \sin \theta_p \cos \phi_p, \sin \theta_p \sin \phi_p, \cos \theta_p), \\ q^\mu &= q_0(1, \sin \theta_q \cos \phi_q, \sin \theta_q \sin \phi_q, \cos \theta_q). \end{aligned} \quad (2.2)$$

Fermions are assumed to be incoming and, if necessary, turned into outgoing ones by crossing, which is performed by inverting the corresponding fermion momenta and helicities. If spinor products appear with negative momenta $-p, -q$ as arguments, it is understood that only the complex conjugate spinor products get the corresponding sign change. We illustrate this by simple examples:

$$\begin{aligned} A(p, q) = \langle pq \rangle &= A(p, -q) = A(-p, q) = A(-p, -q), \\ B(p, q) = \langle pq \rangle^* &= -B(p, -q) = -B(-p, q) = B(-p, -q). \end{aligned} \quad (2.3)$$

The denominator parts of the propagators for vector bosons V and fermions F are abbreviated by

$$P_V(p) = \frac{1}{p^2 - M_V^2 + iM_V \Gamma_V(p^2)}, \quad P_F(p) = \frac{1}{p^2 - m_F^2 + im_F \Gamma_F(p^2)}, \quad (2.4)$$

where the fermion mass m_F is only non-zero for the top quark. The introduction of finite decay widths $\Gamma_V(p^2)$ and $\Gamma_F(p^2)$ in the propagators is described below. Moreover, we introduce abbreviations for sums of external momenta,

$$p_{ab} = p_a + p_b, \quad p_{abc} = p_a + p_b + p_c, \quad p_{abcd} = p_a + p_b + p_c + p_d. \quad (2.5)$$

For the Feynman rules and coupling factors we follow the conventions of Ref. [29]. For the gauge-boson self-interactions we define the following constants,

$$\begin{aligned} C_{WW^\mp V} &= C_{WVW^\pm} = \pm g_{VWW}, & V &= \gamma, Z, \\ C_{WWV_1V_2} &= -g_{V_1WW} g_{V_2WW}, & V_{1,2} &= \gamma, Z, \\ C_{WWWW} &= \frac{1}{s_w^2}, \end{aligned} \quad (2.6)$$

with the abbreviations

$$g_{\gamma WW} = 1, \quad g_{ZWW} = -\frac{c_w}{s_w}. \quad (2.7)$$

The sine and cosine of the weak mixing angle are defined by the masses of the Z and W bosons as follows:

$$c_w^2 = 1 - s_w^2 = \frac{M_W^2}{M_Z^2}. \quad (2.8)$$

Here and in the following the fields denoted in the subscripts are assumed to be incoming. If the charge flow does not matter, we simply write W and ϕ instead of W^\pm and ϕ^\pm ; the corresponding coupling is, of course, understood as zero if charge conservation would be violated. For the couplings of scalar to gauge bosons we introduce

$$\begin{aligned} C_{HZZ} &= \frac{M_W}{c_w^2 s_w}, \\ C_{HWW} &= \frac{M_W}{s_w}, \\ C_{\phi\gamma W} &= C_{\phi W\gamma} = -M_W, \\ C_{\phi ZW} &= C_{\phi WZ} = -\frac{s_w M_W}{c_w}, \end{aligned} \quad (2.9)$$

and for the couplings of the electroweak gauge bosons to fermions

$$g_{\gamma \bar{f}_i f_i}^\sigma = -Q_i, \quad g_{Z \bar{f}_i f_i}^\sigma = -\frac{s_w}{c_w} Q_i + \frac{I_{w,i}^3}{c_w s_w} \delta_{\sigma,-}, \quad g_{W \bar{f}_i f'_i}^\sigma = \frac{1}{\sqrt{2} s_w} \delta_{\sigma,-}, \quad (2.10)$$

where Q_i and $I_{w,i}^3 = \pm 1/2$ denote the relative charge and the weak isospin of the fermion f_i , respectively. The field f'_i corresponds to the weak-isospin partner of f_i . For the gluon coupling to quarks q we introduce

$$g_{g\bar{q}q}^\sigma = \frac{g_s}{e}, \quad (2.11)$$

where $g_s = \sqrt{4\pi\alpha_s}$ is the strong gauge coupling and $e = \sqrt{4\pi\alpha}$ is the electromagnetic coupling. The factor e in the denominator is introduced, because we will separate the global factor e^6 from the $e^+e^- \rightarrow 6f$ helicity amplitudes. By convention, the colour

operator as well as the colour indices of external quarks are split off from the generic amplitudes given below; the whole colour structure will be reinserted when squaring the amplitudes. Finally, we need the Yukawa coupling of the top quark, for which we define

$$g_{\phi\bar{b}t}^\sigma = \frac{m_t}{\sqrt{2}s_w M_W} \delta_{\sigma,+}, \quad g_{\phi\bar{t}b}^\sigma = \frac{m_t}{\sqrt{2}s_w M_W} \delta_{\sigma,-}. \quad (2.12)$$

If any of the constants C_{\dots} or g_{\dots}^σ appears in the following with subscripts not listed here, it is understood to vanish.

The amplitudes for the generic graphs with 4 fermion currents (see Figure 1) are given by

$$\begin{aligned} \mathcal{M}_{(4a)}^{\sigma_a, \dots, \sigma_h}(p_a, \dots, p_h) &= 4e^6 \delta_{\sigma_a,+} \delta_{\sigma_b,-} \delta_{\sigma_c,+} \delta_{\sigma_d,-} \delta_{\sigma_e,-\sigma_f} \delta_{\sigma_g,-\sigma_h} \\ &\times g_{W\bar{f}_a f_b}^- g_{W\bar{f}_c f_d}^- g_{V_1 \bar{f}_e f_f}^{\sigma_f} g_{V_2 \bar{f}_g f_h}^{\sigma_h} C_{WWV_1 V_2} \\ &\times P_W(p_{ab}) P_W(p_{cd}) P_{V_1}(p_{ef}) P_{V_2}(p_{gh}) \\ &\times A_{(4a)}^{\sigma_a, \sigma_c, \sigma_e, \sigma_g}(p_a, \dots, p_h), \end{aligned} \quad (2.13)$$

$$\begin{aligned} \mathcal{M}_{(4b)}^{\sigma_a, \dots, \sigma_h}(p_a, \dots, p_h) &= 4e^6 \delta_{\sigma_a,+} \delta_{\sigma_b,-} \delta_{\sigma_c,-\sigma_d} \delta_{\sigma_e,+} \delta_{\sigma_f,-} \delta_{\sigma_g,-\sigma_h} \\ &\times g_{W\bar{f}_a f_b}^- g_{V_1 \bar{f}_c f_d}^{\sigma_d} g_{W\bar{f}_e f_f}^- g_{V_2 \bar{f}_g f_h}^{\sigma_h} C_{WV_1 V_3} C_{WV_2 V_3} \\ &\times P_W(p_{ab}) P_{V_1}(p_{cd}) P_W(p_{ef}) P_{V_2}(p_{gh}) P_{V_3}(p_{abcd}) \\ &\times A_{(4b)}^{\sigma_a, \sigma_c, \sigma_e, \sigma_g}(p_a, \dots, p_h), \end{aligned} \quad (2.14)$$

$$\begin{aligned} \mathcal{M}_{(4c)}^{\sigma_a, \dots, \sigma_h}(p_a, \dots, p_h) &= -4e^6 \delta_{\sigma_a,-\sigma_b} \delta_{\sigma_c,-\sigma_d} \delta_{\sigma_e,-\sigma_f} \delta_{\sigma_g,-\sigma_h} \\ &\times g_{V_1 \bar{f}_a f_b}^{\sigma_b} g_{V_2 \bar{f}_c f_d}^{\sigma_d} g_{V_3 \bar{f}_e f_f}^{\sigma_f} g_{V_4 \bar{f}_g f_h}^{\sigma_h} C_{SV_1 V_2} C_{SV_3 V_4} \\ &\times P_{V_1}(p_{ab}) P_{V_2}(p_{cd}) P_{V_3}(p_{ef}) P_{V_4}(p_{gh}) P_S(p_{abcd}) \\ &\times A_{(4c)}^{\sigma_a, \sigma_c, \sigma_e, \sigma_g}(p_a, \dots, p_h), \end{aligned} \quad (2.15)$$

where the auxiliary functions A_{\dots} contain the WvdW spinor products. Explicit results for the auxiliary functions read

$$\begin{aligned} A_{(4a)}^{++++}(p_a, \dots, p_h) &= 2\langle p_b p_d \rangle^* \langle p_f p_h \rangle^* \langle p_a p_c \rangle \langle p_e p_g \rangle - \langle p_b p_f \rangle^* \langle p_d p_h \rangle^* \langle p_a p_e \rangle \langle p_c p_g \rangle \\ &\quad - \langle p_b p_h \rangle^* \langle p_d p_f \rangle^* \langle p_a p_g \rangle \langle p_c p_e \rangle, \end{aligned} \quad (2.16)$$

$$\begin{aligned} A_{(4b)}^{++++}(p_a, \dots, p_h) &= \langle p_b p_d \rangle^* \langle p_f p_h \rangle^* \langle p_a p_c \rangle \langle p_e p_g \rangle (p_{ab} - p_{cd}) \cdot (p_{ef} - p_{gh}) \\ &\quad + 2\langle p_b p_d \rangle^* \langle p_a p_c \rangle \left[\langle p_f P_{ab} p_e \rangle \langle p_h P_{cd} p_g \rangle - \langle p_f P_{cd} p_e \rangle \langle p_h P_{ab} p_g \rangle \right] \\ &\quad + 2\langle p_f p_h \rangle^* \langle p_e p_g \rangle \left[\langle p_b P_{ef} p_a \rangle \langle p_d P_{gh} p_c \rangle - \langle p_b P_{gh} p_a \rangle \langle p_d P_{ef} p_c \rangle \right] \\ &\quad + 2\langle p_b P_{cd} p_a \rangle \left[\langle p_d p_h \rangle^* \langle p_c p_g \rangle \langle p_f P_{gh} p_e \rangle - \langle p_d p_f \rangle^* \langle p_c p_e \rangle \langle p_h P_{ef} p_g \rangle \right] \\ &\quad - 2\langle p_d P_{ab} p_c \rangle \left[\langle p_b p_h \rangle^* \langle p_a p_g \rangle \langle p_f P_{gh} p_e \rangle - \langle p_b p_f \rangle^* \langle p_a p_e \rangle \langle p_h P_{ef} p_g \rangle \right], \end{aligned} \quad (2.17)$$

$$A_{(4c)}^{++++}(p_a, \dots, p_h) = \langle p_b p_d \rangle^* \langle p_f p_h \rangle^* \langle p_a p_c \rangle \langle p_e p_g \rangle. \quad (2.18)$$

Here the dot in the first line of Eq. (2.17) indicates the usual Lorentz product of four-vectors, and the extended brackets are shorthands for the expressions

$$\langle p_a P_{bc} p_d \rangle = \langle p_b p_a \rangle^* \langle p_b p_d \rangle + \langle p_c p_a \rangle^* \langle p_c p_d \rangle. \quad (2.19)$$

The remaining helicity configurations of the auxiliary functions follow from discrete symmetries. All non-vanishing $A_{(4...)}^{\sigma_a, \sigma_c, \sigma_e, \sigma_g}$ are obtained from Eqs. (2.16)–(2.18) by the simple substitutions

$$\begin{aligned} A_{(4...)}^{-\sigma_a, \sigma_c, \sigma_e, \sigma_g}(p_a, p_b, p_c, p_d, p_e, p_f, p_g, p_h) &= A_{(4...)}^{\sigma_a, \sigma_c, \sigma_e, \sigma_g}(p_b, p_a, p_c, p_d, p_e, p_f, p_g, p_h), \\ A_{(4...)}^{\sigma_a, -\sigma_c, \sigma_e, \sigma_g}(p_a, p_b, p_c, p_d, p_e, p_f, p_g, p_h) &= A_{(4...)}^{\sigma_a, \sigma_c, \sigma_e, \sigma_g}(p_a, p_b, p_d, p_c, p_e, p_f, p_g, p_h), \\ A_{(4...)}^{\sigma_a, \sigma_c, -\sigma_e, \sigma_g}(p_a, p_b, p_c, p_d, p_e, p_f, p_g, p_h) &= A_{(4...)}^{\sigma_a, \sigma_c, \sigma_e, \sigma_g}(p_a, p_b, p_c, p_d, p_f, p_e, p_g, p_h), \\ A_{(4...)}^{\sigma_a, \sigma_c, \sigma_e, -\sigma_g}(p_a, p_b, p_c, p_d, p_e, p_f, p_g, p_h) &= A_{(4...)}^{\sigma_a, \sigma_c, \sigma_e, \sigma_g}(p_a, p_b, p_c, p_d, p_e, p_f, p_h, p_g). \end{aligned} \quad (2.20)$$

Another useful relation is provided by the fact that taking the complex conjugate of $A_{(4...)}^{\sigma_a, \sigma_c, \sigma_e, \sigma_g}$ reverses all helicities,

$$A_{(4...)}^{-\sigma_a, -\sigma_c, -\sigma_e, -\sigma_g}(p_a, \dots, p_h) = \left(A_{(4...)}^{\sigma_a, \sigma_c, \sigma_e, \sigma_g}(p_a, \dots, p_h) \right)^*, \quad (2.21)$$

which is useful for checking the amplitudes. For the class of diagrams with 4 fermion currents it is obvious that we have helicity conservation for the respective (massless) fermion–antifermion pairs, i.e. each diagram only contributes if

$$\sigma_a = -\sigma_b, \quad \sigma_c = -\sigma_d, \quad \sigma_e = -\sigma_f, \quad \sigma_g = -\sigma_h. \quad (2.22)$$

The amplitudes for the generic graphs with 3 fermion currents (see Figure 2) are given by

$$\begin{aligned} \mathcal{M}_{(3a)}^{\sigma_a, \dots, \sigma_h}(p_a, \dots, p_h) &= 8e^6 \delta_{\sigma_a, -\sigma_b} \delta_{\sigma_c, -\sigma_d} \delta_{\sigma_e, -\sigma_f} \delta_{\sigma_g, -\sigma_h} \\ &\quad \times g_{V_1 \bar{f}_a F_1}^{-\sigma_a} g_{V_3 \bar{F}_2 f_b}^{\sigma_b} g_{V_1 \bar{f}_c f_d}^{\sigma_d} g_{V_2 \bar{f}_e f_f}^{\sigma_f} g_{V_3 \bar{f}_g f_h}^{\sigma_h} \\ &\quad \times P_{F_1}(p_{acd}) P_{F_2}(p_{bgh}) P_{V_1}(p_{cd}) P_{V_2}(p_{ef}) P_{V_3}(p_{gh}) \\ &\quad \times \sum_{\tau=\pm} g_{V_2 \bar{F}_1 F_2}^{\tau} A_{(3a), \tau}^{\sigma_a, \sigma_c, \sigma_e, \sigma_g}(p_a, \dots, p_h), \end{aligned} \quad (2.23)$$

$$\begin{aligned} \mathcal{M}_{(3b)}^{\sigma_a, \dots, \sigma_h}(p_a, \dots, p_h) &= -4e^6 \delta_{\sigma_a, -\sigma_b} \delta_{\sigma_c, -\sigma_d} \delta_{\sigma_e, +\sigma_f} \delta_{\sigma_g, -\sigma_h} \\ &\quad \times g_{V_1 \bar{f}_a F}^{-\sigma_a} g_{V_2 \bar{F} f_b}^{\sigma_b} g_{V_1 \bar{f}_c f_d}^{\sigma_d} g_{W \bar{f}_e f_f}^{-\sigma_f} g_{V_3 \bar{f}_g f_h}^{\sigma_h} C_{WV_2 V_3} \\ &\quad \times P_F(p_{acd}) P_{V_1}(p_{cd}) P_{V_2}(p_{efgh}) P_W(p_{ef}) P_{V_3}(p_{gh}) \\ &\quad \times A_{(3b)}^{\sigma_a, \sigma_c, \sigma_e, \sigma_g}(p_a, \dots, p_h), \end{aligned} \quad (2.24)$$

$$\begin{aligned} \mathcal{M}_{(3c)}^{\sigma_a, \dots, \sigma_h}(p_a, \dots, p_h) &= -4e^6 \delta_{\sigma_a, -\sigma_b} \delta_{\sigma_c, -\sigma_d} \delta_{\sigma_e, +\sigma_f} \delta_{\sigma_g, -\sigma_h} \\ &\quad \times g_{V_2 \bar{f}_a F}^{-\sigma_a} g_{V_1 \bar{F} f_b}^{\sigma_b} g_{V_1 \bar{f}_c f_d}^{\sigma_d} g_{W \bar{f}_e f_f}^{-\sigma_f} g_{V_3 \bar{f}_g f_h}^{\sigma_h} C_{WV_2 V_3} \\ &\quad \times P_F(p_{bcd}) P_{V_1}(p_{cd}) P_{V_2}(p_{efgh}) P_W(p_{ef}) P_{V_3}(p_{gh}) \\ &\quad \times A_{(3c)}^{\sigma_a, \sigma_c, \sigma_e, \sigma_g}(p_a, \dots, p_h), \end{aligned} \quad (2.25)$$

$$\begin{aligned} \mathcal{M}_{(3d)}^{\sigma_a, \dots, \sigma_h}(p_a, \dots, p_h) &= 4e^6 \delta_{\sigma_a, +\sigma_b} \delta_{\sigma_c, -\sigma_d} \delta_{\sigma_e, +\sigma_f} \delta_{\sigma_g, -\sigma_h} \\ &\quad \times g_{W \bar{f}_a t}^{-\sigma_a} g_{\phi \bar{t} f_b}^{\sigma_b} g_{W \bar{f}_c f_d}^{-\sigma_d} g_{W \bar{f}_e f_f}^{-\sigma_f} g_{V \bar{f}_g f_h}^{\sigma_h} C_{\phi WV} \\ &\quad \times P_t(p_{acd}) P_W(p_{cd}) P_W(p_{efgh}) P_W(p_{ef}) P_V(p_{gh}) \\ &\quad \times A_{(3d)}^{\sigma_a, \sigma_c, \sigma_e, \sigma_g}(p_a, \dots, p_h), \end{aligned} \quad (2.26)$$

$$\begin{aligned}
\mathcal{M}_{(3e)}^{\sigma_a, \dots, \sigma_h}(p_a, \dots, p_h) &= 4e^6 \delta_{\sigma_a, +} \delta_{\sigma_b, -} \delta_{\sigma_c, +} \delta_{\sigma_d, -} \delta_{\sigma_e, +} \delta_{\sigma_f, -} \delta_{\sigma_g, -} \delta_{\sigma_h} \\
&\times g_{\phi \bar{f}_a t}^+ g_{\bar{W} \bar{t} f_b} g_{\bar{W} \bar{f}_c f_d} g_{\bar{W} \bar{f}_e f_f} g_{V \bar{f}_g f_h}^{\sigma_h} C_{\phi W V} \\
&\times P_t(p_{bcd}) P_W(p_{cd}) P_W(p_{efgh}) P_W(p_{ef}) P_V(p_{gh}) \\
&\times A_{(3e)}^{\sigma_a, \sigma_c, \sigma_e, \sigma_g}(p_a, \dots, p_h). \tag{2.27}
\end{aligned}$$

At first sight it seems that the occurrence of a top quark in the spinor chain between f_a and f_b can violate helicity conservation in this line. However, this is not true since the top-quark propagator always appears between two chirality projectors, restoring helicity conservation in the whole fermion line. Thus, as in the case of 4 fermion currents all graphs with 3 fermion currents vanish if Eq. (2.22) is not fulfilled. We have already made use of Eq. (2.22) in the expressions for the matrix elements Eqs. (2.23)–(2.27). The auxiliary functions A_{\dots} read

$$\begin{aligned}
A_{(3a),+}^{++++}(p_a, \dots, p_h) &= -m_{F_1} m_{F_2} \langle p_b p_h \rangle^* \langle p_d p_f \rangle^* \langle p_a p_c \rangle \langle p_e p_g \rangle, \\
A_{(3a),-}^{++++}(p_a, \dots, p_h) &= -\langle p_b p_h \rangle^* \langle p_a p_c \rangle \langle p_d P_{ac} p_e \rangle \langle p_f P_{bh} p_g \rangle, \tag{2.28}
\end{aligned}$$

$$\begin{aligned}
A_{(3b)}^{++++}(p_a, \dots, p_h) &= \langle p_a p_c \rangle \left\{ \langle p_f p_h \rangle^* \langle p_e p_g \rangle \left[\langle p_a p_d \rangle^* \left(\langle p_b P_{ef} p_a \rangle - \langle p_b P_{gh} p_a \rangle \right) \right. \right. \\
&\quad \left. \left. + \langle p_c p_d \rangle^* \left(\langle p_b P_{ef} p_c \rangle - \langle p_b P_{gh} p_c \rangle \right) \right] \right. \\
&\quad \left. + 2 \langle p_b p_h \rangle^* \langle p_d P_{ac} p_g \rangle \langle p_f P_{gh} p_e \rangle \right. \\
&\quad \left. - 2 \langle p_b p_f \rangle^* \langle p_d P_{ac} p_e \rangle \langle p_h P_{ef} p_g \rangle \right\}, \tag{2.29}
\end{aligned}$$

$$\begin{aligned}
A_{(3c)}^{++++}(p_a, \dots, p_h) &= \langle p_b p_d \rangle^* \left\{ \langle p_f p_h \rangle^* \langle p_e p_g \rangle \left[-\langle p_b p_c \rangle \left(\langle p_b P_{ef} p_a \rangle - \langle p_b P_{gh} p_a \rangle \right) \right. \right. \\
&\quad \left. \left. + \langle p_c p_d \rangle \left(\langle p_d P_{ef} p_a \rangle - \langle p_d P_{gh} p_a \rangle \right) \right] \right. \\
&\quad \left. - 2 \langle p_a p_g \rangle \langle p_h P_{bd} p_c \rangle \langle p_f P_{gh} p_e \rangle \right. \\
&\quad \left. + 2 \langle p_a p_e \rangle \langle p_f P_{bd} p_c \rangle \langle p_h P_{ef} p_g \rangle \right\}, \tag{2.30}
\end{aligned}$$

$$A_{(3d)}^{++++}(p_a, \dots, p_h) = A_{(3e)}^{++++}(p_a, \dots, p_h) = m_t \langle p_b p_d \rangle^* \langle p_f p_h \rangle^* \langle p_a p_c \rangle \langle p_e p_g \rangle, \tag{2.31}$$

where the expressions for the remaining polarizations are again obtained by simple substitutions,

$$\begin{aligned}
A_{(3...),\tau}^{\sigma_a, -\sigma_c, \sigma_e, \sigma_g}(p_a, p_b, p_c, p_d, p_e, p_f, p_g, p_h) &= A_{(3...),\tau}^{\sigma_a, \sigma_c, \sigma_e, \sigma_g}(p_a, p_b, p_d, p_c, p_e, p_f, p_g, p_h), \\
A_{(3...),\tau}^{\sigma_a, \sigma_c, -\sigma_e, \sigma_g}(p_a, p_b, p_c, p_d, p_e, p_f, p_g, p_h) &= A_{(3...),\tau}^{\sigma_a, \sigma_c, \sigma_e, \sigma_g}(p_a, p_b, p_c, p_d, p_f, p_e, p_g, p_h), \\
A_{(3...),\tau}^{\sigma_a, \sigma_c, \sigma_e, -\sigma_g}(p_a, p_b, p_c, p_d, p_e, p_f, p_g, p_h) &= A_{(3...),\tau}^{\sigma_a, \sigma_c, \sigma_e, \sigma_g}(p_a, p_b, p_c, p_d, p_e, p_f, p_h, p_g), \\
A_{(3...),-\tau}^{-\sigma_a, -\sigma_c, -\sigma_e, -\sigma_g}(p_a, \dots, p_h) &= \left(A_{(3...),\tau}^{\sigma_a, \sigma_c, \sigma_e, \sigma_g}(p_a, \dots, p_h) \right)^* \Big|_{m_t^* \rightarrow m_t}, \tag{2.32}
\end{aligned}$$

where the index τ has to be ignored for all functions other than $A_{(3a),\tau}$ and the substitution $m_t^* \rightarrow m_t$ ensures that the top-quark mass (if taken complex) remains unaffected by the complex conjugation.

The amplitudes for the generic graphs with 2 fermion currents (see Figure 3) are given by

$$\mathcal{M}_{(2a)}^{\sigma_a, \dots, \sigma_h}(p_a, \dots, p_h) = 8e^6 \delta_{\sigma_a, -\sigma_b} \delta_{\sigma_c, -\sigma_d} \delta_{\sigma_e, -\sigma_f} \delta_{\sigma_g, -\sigma_h}$$

$$\begin{aligned}
& \times g_{V_1 \bar{f}_a F_1}^{-\sigma_a} g_{V_2 \bar{F}_1 f_b}^{\sigma_b} g_{V_2 \bar{f}_c F_2}^{-\sigma_c} g_{V_3 \bar{F}_2 f_d}^{\sigma_d} g_{V_1 \bar{f}_e f_f}^{\sigma_f} g_{V_3 \bar{f}_g f_h}^{\sigma_h} \\
& \times P_{F_1}(p_{aef}) P_{F_2}(p_{dgh}) P_{V_1}(p_{ef}) P_{V_2}(p_{abef}) P_{V_3}(p_{gh}) \\
& \times A_{(2a)}^{\sigma_a, \sigma_c, \sigma_e, \sigma_g}(p_a, \dots, p_h), \tag{2.33}
\end{aligned}$$

$$\begin{aligned}
\mathcal{M}_{(2b)}^{\sigma_a, \dots, \sigma_h}(p_a, \dots, p_h) &= 8e^6 \delta_{\sigma_a, -\sigma_b} \delta_{\sigma_c, -\sigma_d} \delta_{\sigma_e, -\sigma_f} \delta_{\sigma_g, -\sigma_h} \\
& \times g_{V_1 \bar{f}_a F_1}^{-\sigma_a} g_{V_2 \bar{F}_1 f_b}^{\sigma_b} g_{V_3 \bar{f}_c F_2}^{-\sigma_c} g_{V_2 \bar{F}_2 f_d}^{\sigma_d} g_{V_1 \bar{f}_e f_f}^{\sigma_f} g_{V_3 \bar{f}_g f_h}^{\sigma_h} \\
& \times P_{F_1}(p_{aef}) P_{F_2}(p_{cgh}) P_{V_1}(p_{ef}) P_{V_2}(p_{abef}) P_{V_3}(p_{gh}) \\
& \times A_{(2b)}^{\sigma_a, \sigma_c, \sigma_e, \sigma_g}(p_a, \dots, p_h), \tag{2.34}
\end{aligned}$$

$$\begin{aligned}
\mathcal{M}_{(2c)}^{\sigma_a, \dots, \sigma_h}(p_a, \dots, p_h) &= 8e^6 \delta_{\sigma_a, -\sigma_b} \delta_{\sigma_c, -\sigma_d} \delta_{\sigma_e, -\sigma_f} \delta_{\sigma_g, -\sigma_h} \\
& \times g_{V_2 \bar{f}_a F_1}^{-\sigma_a} g_{V_1 \bar{F}_1 f_b}^{\sigma_b} g_{V_2 \bar{f}_c F_2}^{-\sigma_c} g_{V_3 \bar{F}_2 f_d}^{\sigma_d} g_{V_1 \bar{f}_e f_f}^{\sigma_f} g_{V_3 \bar{f}_g f_h}^{\sigma_h} \\
& \times P_{F_1}(p_{bef}) P_{F_2}(p_{dgh}) P_{V_1}(p_{ef}) P_{V_2}(p_{abef}) P_{V_3}(p_{gh}) \\
& \times A_{(2c)}^{\sigma_a, \sigma_c, \sigma_e, \sigma_g}(p_a, \dots, p_h), \tag{2.35}
\end{aligned}$$

$$\begin{aligned}
\mathcal{M}_{(2d)}^{\sigma_a, \dots, \sigma_h}(p_a, \dots, p_h) &= 4e^6 \delta_{\sigma_a, +\sigma_b, -\sigma_c, +\sigma_d, -\sigma_e, +\sigma_f, -\sigma_g, +\sigma_h, -} \\
& \times g_{W \bar{f}_a t}^{-\sigma_a} g_{\phi \bar{t} f_b}^{\sigma_b} g_{\phi \bar{f}_c t}^{\sigma_c} g_{W \bar{t} f_d}^{-\sigma_d} g_{W \bar{f}_e f_f}^{\sigma_e} g_{W \bar{f}_g f_h}^{\sigma_h} \\
& \times P_t(p_{aef}) P_t(p_{dgh}) P_W(p_{ef}) P_W(p_{abef}) P_W(p_{gh}) \\
& \times A_{(2d)}^{\sigma_a, \sigma_c, \sigma_e, \sigma_g}(p_a, \dots, p_h). \tag{2.36}
\end{aligned}$$

Again we exploited the fact that helicity conservation in each spinor chain containing top quarks is restored by chirality projectors, i.e. that Eq. (2.22) is necessary for non-vanishing contributions. The functions A_{\dots} read

$$\begin{aligned}
A_{(2a)}^{++++}(p_a, \dots, p_h) &= \langle p_d p_h \rangle^* \langle p_a p_e \rangle \langle p_b P_{dh} p_g \rangle \langle p_f P_{ae} p_c \rangle, \\
A_{(2a)}^{-+++}(p_a, \dots, p_h) &= \langle p_a p_f \rangle^* \langle p_d p_h \rangle^* \langle p_b p_c \rangle \left[\langle p_a p_e \rangle \langle p_a P_{dh} p_g \rangle - \langle p_e p_f \rangle \langle p_f P_{dh} p_g \rangle \right], \tag{2.37}
\end{aligned}$$

$$\begin{aligned}
A_{(2b)}^{++++}(p_a, \dots, p_h) &= -\langle p_b p_d \rangle^* \langle p_a p_e \rangle \langle p_c p_g \rangle \left[\langle p_a p_f \rangle^* \langle p_h P_{cg} p_a \rangle + \langle p_e p_f \rangle^* \langle p_h P_{cg} p_e \rangle \right], \\
A_{(2b)}^{-+++}(p_a, \dots, p_h) &= -\langle p_a p_f \rangle^* \langle p_c p_g \rangle \langle p_d P_{af} p_e \rangle \langle p_h P_{cg} p_b \rangle, \tag{2.38}
\end{aligned}$$

$$\begin{aligned}
A_{(2c)}^{++++}(p_a, \dots, p_h) &= -\langle p_b p_f \rangle^* \langle p_d p_h \rangle^* \langle p_a p_c \rangle \left[\langle p_b p_e \rangle \langle p_b P_{dh} p_g \rangle - \langle p_e p_f \rangle \langle p_f P_{dh} p_g \rangle \right], \\
A_{(2c)}^{-+++}(p_a, \dots, p_h) &= -\langle p_d p_h \rangle^* \langle p_b p_e \rangle \langle p_a P_{dh} p_g \rangle \langle p_f P_{be} p_c \rangle, \tag{2.39}
\end{aligned}$$

$$A_{(2d)}^{++++}(p_a, \dots, p_h) = -m_t^2 \langle p_b p_f \rangle^* \langle p_d p_h \rangle^* \langle p_a p_e \rangle \langle p_c p_g \rangle, \tag{2.40}$$

with the following substitutions for the remaining polarizations,

$$\begin{aligned}
A_{(2\dots)}^{\sigma_a, \sigma_c, -\sigma_e, \sigma_g}(p_a, p_b, p_c, p_d, p_e, p_f, p_g, p_h) &= A_{(2\dots)}^{\sigma_a, \sigma_c, \sigma_e, \sigma_g}(p_a, p_b, p_c, p_d, p_f, p_e, p_g, p_h), \\
A_{(2\dots)}^{\sigma_a, \sigma_c, \sigma_e, -\sigma_g}(p_a, p_b, p_c, p_d, p_e, p_f, p_g, p_h) &= A_{(2\dots)}^{\sigma_a, \sigma_c, \sigma_e, \sigma_g}(p_a, p_b, p_c, p_d, p_e, p_f, p_h, p_g), \\
A_{(2\dots)}^{-\sigma_a, -\sigma_c, -\sigma_e, -\sigma_g}(p_a, \dots, p_h) &= \left(A_{(2\dots)}^{\sigma_a, \sigma_c, \sigma_e, \sigma_g}(p_a, \dots, p_h) \right)^* \Big|_{m_t^* \rightarrow m_t}. \tag{2.41}
\end{aligned}$$

2.2 Squared matrix elements from generic amplitudes

Having defined all amplitudes involving 8 external massless fermions in the previous section, we now turn to the evaluation of the squared matrix elements for a given process

$2f \rightarrow 6f$. Since the adopted approach is based on helicity eigenstates of the external fermions, in a first step we calculate the squares of all helicity matrix elements and take the incoherent sum over the relevant helicity configurations at the end. We widely suppress the helicity labels in the following.

The fermion lines with an outgoing arrow are enumerated by $i = 1, 3, 5, 7$; they correspond to incoming antifermions \bar{f}_i or outgoing fermions f_i . The fermion lines with an incoming arrow are enumerated by $i = 2, 4, 6, 8$; they correspond to incoming fermions f_i or outgoing antifermions \bar{f}_i . The respective incoming momenta and helicities are denoted by p_i and σ_i , i.e. these quantities receive a minus sign by crossing if they belong to final-state particles. For instance, for a scattering reaction of the incoming $\bar{f}_7 f_8$ pair, our notation is

$$\begin{aligned} \bar{f}_7(p_7, \sigma_7) + f_8(p_8, \sigma_8) \rightarrow & f_1(-p_1, -\sigma_1) + \bar{f}_2(-p_2, -\sigma_2) + f_3(-p_3, -\sigma_3) \\ & + \bar{f}_4(-p_4, -\sigma_4) + f_5(-p_5, -\sigma_5) + \bar{f}_6(-p_6, -\sigma_6), \end{aligned} \quad (2.42)$$

where the momenta and helicities within parentheses correspond to incoming fields, i.e. they are identified with appropriate permutations of the momenta p_a, \dots, p_h and helicities $\sigma_a, \dots, \sigma_h$ in the generic amplitudes $\mathcal{M}_{(\dots)}^{\sigma_a, \dots, \sigma_h}(p_a, \dots, p_h)$ of the previous section. Finally, all relevant Feynman graphs have to be summed and squared taking into account colour correlations.

In detail the construction proceeds in three steps:

(i) *Fermion permutations*

First we write down all permutations of $(1, 3, 5, 7)$ and $(2, 4, 6, 8)$ for (a, c, e, g) and (b, d, f, h) , respectively, resulting in $(4!)^2 = 576$ different combinations (a, \dots, h) . The generic amplitudes vanish if at least one of the pairs $\bar{f}_a f_b$, $\bar{f}_c f_d$, $\bar{f}_e f_f$, and $\bar{f}_g f_h$ does not appear in a vertex $V \bar{f} f$ with a gauge boson V . Therefore, we can omit such combinations (a, \dots, h) from the beginning. This excludes, for instance, combinations where at least one of the pairs consists of a lepton and a quark. However, there are also channels, such as $e^+ e^- \rightarrow e^+ e^- e^+ e^- e^+ e^-$, where all 576 combinations contribute. In the following we enumerate the relevant combinations by $n = 1, \dots, N$ ($N \leq 576$) and denote them by (a_n, \dots, h_n) . Next we determine the relative sign factors η_n between diagrams that differ in their fermion-number flow by an interchange of external lines. Obviously

$$\eta_n = \epsilon_{a_n, \dots, h_n} = \begin{cases} +1 & \text{for even permutations } (a_n, \dots, h_n) \text{ of } (1, \dots, 8), \\ -1 & \text{for odd permutations } (a_n, \dots, h_n) \text{ of } (1, \dots, 8), \\ 0 & \text{otherwise,} \end{cases} \quad (2.43)$$

yields the correct signs.

(ii) *Amplitude evaluation*

In the next step we evaluate the generic amplitudes $\mathcal{M}_{(\dots)}^{\sigma_a, \dots, \sigma_h}(p_a, \dots, p_h)$ with the identifications $(a, \dots, h) = (a_n, \dots, h_n)$, i.e. we calculate all graphs shown in Figures 1–3 with all possible internal bosons. More precisely, in order to avoid double counting we require appropriate conditions for (a, \dots, h) and the internal bosons to ensure that each Feynman diagram is calculated only once. These conditions are listed in Table 1, where

Amplitude	Bosons	Fermions	Charge flow
4a	$V_{\{1,2\}} = \{W, W\}$	$a < c, e < g$	$Q_{ab} = Q_{cd} = -1$
	$V_{\{1,2\}} = \{\gamma/Z, \gamma/Z\}$	$e < g$	$Q_{ab} = -1$
4b	$V_{\{1,2,3\}} = \{W, W, \gamma/Z\}$	$a < g$	$Q_{ab} = Q_{gh} = -1$
	$V_{\{1,2,3\}} = \{\gamma/Z, \gamma/Z, W\}$	none	$Q_{ab} = -1$
4c	$V_{\{1,2,3,4\}} = \{W, W, W, W\}, S = H$	$a < g$	$Q_{ab} = Q_{gh} = -1$
	$V_{\{1,2,3,4\}} = \{W, W, Z, Z\}, S = H$	$e < g$	$Q_{ab} = -1$
	$V_{\{1,2,3,4\}} = \{Z, Z, Z, Z\}, S = H$	$a = 1, e < g$	none
	$V_{\{1,2,3,4\}} = \{W, \gamma/Z, W, \gamma/Z\}, S = \phi$	none	$Q_{ab} = -1$
3b, 3c	$V_{\{1,2,3\}} = \{W, W, \gamma/Z\}$	none	none
	$V_{\{1,2,3\}} = \{W, \gamma/Z, W\}$	none	$Q_{ef} = -1$
	$V_{\{1,2,3\}} = \{\gamma/Z/g, W, \gamma/Z\}$	none	none
	$V_{\{1,2,3\}} = \{\gamma/Z/g, \gamma/Z, W\}$	none	$Q_{ef} = -1$
2b, 2c	none	$a < c$	none
3a, 3d, 3e, 2a, 2d	none	none	none

Table 1: Restrictions on the field insertions and on the charge flow in the generic amplitudes (The lists for the field insertions are ordered.)

$Q_{ab} = Q_b - Q_a$ is the total incoming charge of the pair $\bar{f}_a f_b$. An entry “none” means that all insertions allowed by charge conservation are possible. For example, the second line in Table 1 for diagram “4b” means that the vector bosons V_1 and V_2 each can be either a photon or Z boson, V_3 is a W boson with a negative charge $-e$ flowing through the diagram from the $\bar{f}_a f_b$ pair to the $\bar{f}_e f_f$ pair, while no restriction on the numbers a, \dots, h is imposed.

At this stage, we can already sum up diagrams that belong to the same fermion permutation and have the same colour structure. In this way we obtain the sums $\mathcal{M}_n^{(\text{ew})}$ and $\mathcal{M}_n^{(\text{1g})}$ which include all purely electroweak and one-gluon exchange diagrams for (a_n, \dots, h_n) , respectively. Here one should realize that the number of diagrams can be rather large, ranging from typically $\sim 10^2$ – 10^3 up to 13896 for $e^+e^- \rightarrow e^+e^-e^+e^-e^+e^-$.

(iii) *Squared matrix element*

If no external quarks are involved the squared matrix element $|\mathcal{M}_{\text{lept}}|^2$ is simply obtained by squaring the sum over all contributions $\eta_n \mathcal{M}_n^{(\text{ew})}$,

$$|\mathcal{M}_{\text{lept}}|^2 = \left| \sum_{n=1}^N \eta_n \mathcal{M}_n^{(\text{ew})} \right|^2. \quad (2.44)$$

For two external quarks the situation is as simple as in the purely leptonic case. The quark line always closes to the same loop in the squared “interference” diagrams, leading to a global factor 3 from the colour trace,

$$\sum_{\text{colour}} |\mathcal{M}_{2q}|^2 = 3 \left| \sum_{n=1}^N \eta_n \mathcal{M}_n^{(\text{ew})} \right|^2. \quad (2.45)$$

For four external quarks non-trivial colour interferences occur. Denoting the four quarks by $\bar{q}_1 q_2 \bar{q}_3 q_4$, there are two types of diagrams: one type in which the pairs $\bar{q}_1 q_2$ and $\bar{q}_3 q_4$ define the two quark lines, and another one in which $\bar{q}_1 q_4$ and $\bar{q}_3 q_2$ define the lines. According to this criterion we divide the set of N permutations (a_n, \dots, h_n) into two subsets of $N/2$ permutations for each of the two diagram types and label the permutations by the pair of indices (n, α) with $n = 1, \dots, N/2$, $\alpha = 1, 2$ instead of taking $n = 1, \dots, N$. Hence, $\mathcal{M}_{n,\alpha}^{(\text{ew})}$ and $\mathcal{M}_{n,\alpha}^{(\text{1g})}$ denote the sums of purely electroweak and one-gluon diagrams for $(a_{n,\alpha}, \dots, h_{n,\alpha})$, respectively, where the index α determines whether $\bar{q}_1 q_2$ and $\bar{q}_3 q_4$ or $\bar{q}_1 q_4$ and $\bar{q}_3 q_2$ correspond to the two quark lines. The squared matrix element is obtained from terms of the form $\mathcal{M}_{n,\alpha}^{(X)} (\mathcal{M}_{m,\beta}^{(Y)})^*$. If $\alpha = \beta$, diagrammatically such a term represents interference graphs in which the two quark lines close separately; for purely electroweak diagrams ($X = Y = \text{ew}$) each closed quark yields a colour factor 3, leading to a colour factor $3^2 = 9$ for the whole interference term. If $\alpha \neq \beta$, the two quark lines close to a single loop, leading to a colour factor 3 for purely electroweak diagrams. If at least one of the terms $\mathcal{M}_{n,\alpha}^{(X)}$ and $(\mathcal{M}_{m,\beta}^{(Y)})^*$ stands for one-gluon diagrams, the colour factors result from some simple traces over Gell-Mann matrices. We summarize the colour factors in terms of 2×2 matrices $C_{4q}^{(X,Y)}$:

$$C_{4q}^{(\text{ew},\text{ew})} = \begin{pmatrix} 9 & 3 \\ 3 & 9 \end{pmatrix}, \quad C_{4q}^{(\text{1g},\text{1g})} = \begin{pmatrix} 2 & -\frac{2}{3} \\ -\frac{2}{3} & 2 \end{pmatrix}, \quad C_{4q}^{(\text{ew},\text{1g})} = \begin{pmatrix} 0 & 4 \\ 4 & 0 \end{pmatrix}. \quad (2.46)$$

Using these matrices, the squared matrix element reads

$$\begin{aligned} \sum_{\text{colour}} |\mathcal{M}_{4q}|^2 = & \sum_{\alpha,\beta=1}^2 \left(\sum_{n=1}^{N/2} \eta_{n,\alpha} \mathcal{M}_{n,\alpha}^{(\text{ew})} \right) C_{4q,\alpha\beta}^{(\text{ew},\text{ew})} \left(\sum_{m=1}^{N/2} \eta_{m,\beta} \mathcal{M}_{m,\beta}^{(\text{ew})} \right)^* \\ & + \sum_{\alpha,\beta=1}^2 \left(\sum_{n=1}^{N/2} \eta_{n,\alpha} \mathcal{M}_{n,\alpha}^{(\text{1g})} \right) C_{4q,\alpha\beta}^{(\text{1g},\text{1g})} \left(\sum_{m=1}^{N/2} \eta_{m,\beta} \mathcal{M}_{m,\beta}^{(\text{1g})} \right)^* \\ & + 2 \operatorname{Re} \left\{ \sum_{\alpha,\beta=1}^2 \left(\sum_{n=1}^{N/2} \eta_{n,\alpha} \mathcal{M}_{n,\alpha}^{(\text{ew})} \right) C_{4q,\alpha\beta}^{(\text{ew},\text{1g})} \left(\sum_{m=1}^{N/2} \eta_{m,\beta} \mathcal{M}_{m,\beta}^{(\text{1g})} \right)^* \right\}. \end{aligned} \quad (2.47)$$

2.3 Introduction of finite decay widths

For the finite decay widths introduced in the propagator functions (2.4) we provide three possibilities as options:

$$\Gamma(p^2) = \begin{cases} \Gamma, & \text{fixed width,} \\ \Gamma \times \theta(p^2), & \text{step width,} \\ \Gamma \times \frac{p^2}{M^2} \theta(p^2), & \text{running width,} \end{cases} \quad (2.48)$$

where M and Γ denote the mass and on-shell decay width of the propagating particle, respectively, and $\theta(x)$ is the usual step function. In the *fixed-width scheme*, the constant width Γ is introduced in each propagator, s -channel- or t -channel-like, i.e. for time-like and space-like momentum transfer, respectively. In the *step-width scheme* and in the *running-width scheme* only s -channel propagators receive a finite width, as actually demanded from field-theoretical principles, and the factor p^2/M^2 in the running width reproduces the correct momentum dependence of the imaginary part of a one-loop self-energy for a particle that decays into massless decay products.

Note that none of these schemes preserves gauge invariance, as for instance explained in Refs. [2, 27, 30, 31, 32, 33]. Nevertheless for the processes $e^+e^- \rightarrow 4f(+\gamma)$ the gauge-invariance-violating effects in the fixed-width scheme turned out to be sufficiently suppressed [21, 31], rendering this simple scheme very useful. Moreover, it was pointed out in Ref. [21] that gauge invariance is restored in the fixed-width approach if complex gauge-boson masses are used in all Feynman rules,² i.e. in particular the weak mixing angle is derived from the complex gauge-boson masses,

$$c_w^2 = 1 - s_w^2 = \frac{M_W^2 - iM_W\Gamma_W}{M_Z^2 - iM_Z\Gamma_Z}. \quad (2.49)$$

This *complex-mass scheme* is included as a fourth option in LUSIFER.

The so-called *fermion-loop scheme* [31], which introduces gauge-boson widths by a gauge-invariant fermion-loop resummation, is not sufficient for six-fermion production in general and thus not considered in the following, since it does not provide an introduction of the decay widths of the top quark and the Higgs boson, because these particles do not (or not entirely) decay into fermion–antifermion pairs. On the other hand, the effective Lagrangian approach of Ref. [33] or appropriate expansions [30] about resonance poles could also be used for $e^+e^- \rightarrow 6f$ processes, but this task goes beyond the scope of this paper.

2.4 Cross-checks

Apart from performing internal checks, we have compared the squared matrix elements for some phase-space points with the results obtained with MADGRAPH [28]. Since MADGRAPH calculates amplitudes within the unitary gauge without providing a gauge-invariant introduction of decay widths, we performed the comparison for vanishing decay widths consistently. We find very good numerical agreement for non-exceptional phase-space points between our results and the ones of MADGRAPH, whenever the latter program delivers an amplitude. For a recent test version of MADGRAPH, directly obtained from the authors [34], there are only two $e^+e^- \rightarrow 6f$ channels that are not covered, $e^+e^- \rightarrow e^+e^-e^+e^-e^+e^-$ and $e^+e^- \rightarrow e^+e^-e^+e^-\nu_e\bar{\nu}_e$. We note that the amplitude check was done with and without (coherent) inclusion of gluon background diagrams.

²It is not clear whether this scheme, where masses and couplings are complex, is consistent also in higher perturbative orders.

3 Multi-channel phase-space integration

Monte Carlo generators are widely used for experimental analyses since they provide realistic event samples that can be compared with experimental observations after detector simulation. Another advantage of a Monte Carlo generator is its flexibility; all possible observables can be studied easily by choosing suitable separation cuts. However, for a proper use of the Monte Carlo program a basic knowledge of the numerical integration techniques is helpful. Therefore, the numerical integration of LUSIFER is briefly outlined in the following. The general method is very similar to the one used in RACOONWW, as described in Refs. [21, 35], but generalized to six-fermion processes.

For six-fermion production, $e^+e^- \rightarrow 6f$, an integration over a 14-dimensional phase space has to be performed. Denoting the incoming e^\pm momenta p_\pm and the outgoing fermion momenta k_i ($i = 1, \dots, 6$), the phase-space integral reads

$$\begin{aligned} \int d\sigma_{\text{Born}} &= \int d\Phi^{2 \rightarrow 6} \frac{|\mathcal{M}(p_+, p_-, k_1, \dots, k_6)|^2}{8(2\pi)^{14} E_{\text{CM}}^2}, \\ d\Phi^{2 \rightarrow 6} &= \prod_{i=1}^6 \frac{d^3 \mathbf{k}_i}{2k_i^0} \delta^{(4)}\left(p_+ + p_- - \sum_{j=1}^6 k_j\right) \Big|_{k_i^0 = \sqrt{\mathbf{k}_i^2 + m_i^2}}, \end{aligned} \quad (3.1)$$

where the fermion masses m_i are zero in our case ($m_i = 0$) and E_{CM} is the total CM energy. The numerical integration (3.1) is rather complicated owing to the rich peaking structure of the integrand. The amplitude involves a huge number of propagators that become resonant or are enhanced in various phase-space regions. The problem is even more serious if the separation cuts, which are required to exclude infrared and collinear singularities from the physical integration domain, are small.

To obtain reliable numerical results, events have to be sampled more frequently in the integration domains where the integrand is large. This redistribution of events is called *importance sampling*. In practice, this means that the mapping of the pseudo-random numbers r_i , $0 \leq r_i \leq 1$, into the space of final-state momenta has to be chosen such that the corresponding Jacobian $1/g(\mathbf{r})$ cancels the propagators of the differential cross section at least partially:

$$d\Phi^{2 \rightarrow 6} = d^{14} \mathbf{r} \frac{1}{g(\mathbf{r})}. \quad (3.2)$$

3.1 Propagator mappings

In order to smooth a single propagator with momentum transfer q in the square of a matrix element,

$$|\mathcal{M}|^2 \propto \frac{1}{(q^2 - M^2)^2 + M^2 \Gamma^2}, \quad (3.3)$$

the phase space is parametrized in such a way that the virtuality q^2 of the propagator is chosen as an integration variable. The integral over q^2 is transformed into an integral over the random number r :

$$\int_{q_{\text{min}}^2}^{q_{\text{max}}^2} dq^2 = \int_0^1 dr \frac{1}{g_{\text{prop}}(q^2(r))}. \quad (3.4)$$

The dependence of q^2 on the pseudo-random number r has to be chosen such that the Jacobian $1/g_{\text{prop}}$ smoothes the propagator (3.3). In LUSIFER two types of mappings are used according to the mass M of the propagating particle. Since all occurring massive particles possess a finite decay width Γ , a suitable mapping is of Breit–Wigner type ($M \neq 0, \Gamma \neq 0$):

$$\begin{aligned} q^2(r) &= M\Gamma \tan[y_1 + (y_2 - y_1)r] + M^2, \\ g_{\text{prop}}(q^2) &= \frac{M\Gamma}{(y_2 - y_1)[(q^2 - M^2)^2 + M^2\Gamma^2]} \end{aligned} \quad (3.5)$$

with

$$y_{1,2} = \arctan\left(\frac{q_{\text{min,max}}^2 - M^2}{M\Gamma}\right). \quad (3.6)$$

For massless particles the following mappings are appropriate ($M = \Gamma = 0$):

$$\begin{aligned} q^2(r) &= \left[r(q_{\text{max}}^2)^{1-\nu} + (1-r)(q_{\text{min}}^2)^{1-\nu}\right]^{\frac{1}{1-\nu}}, \\ g_{\text{prop}}(q^2) &= \frac{1-\nu}{(q^2)^\nu [(q_{\text{max}}^2)^{1-\nu} - (q_{\text{min}}^2)^{1-\nu}]}; \end{aligned} \quad (3.7)$$

$$\begin{aligned} q^2(r) &= (q_{\text{max}}^2)^r (q_{\text{min}}^2)^{1-r}, \\ g_{\text{prop}}(q^2) &= \frac{1}{q^2 \ln(q_{\text{max}}^2/q_{\text{min}}^2)}. \end{aligned} \quad (3.8)$$

The mapping (3.7) is only valid for $\nu \neq 1$, while Eq. (3.8) is a substitute of Eq. (3.7) for $\nu = 1$. The naive expectation $\nu = 2$ from the squared matrix element is not necessarily the best choice because the propagator poles are partially cancelled in the collinear limit. It turns out that a proper value is $\nu \lesssim 1$.

3.2 Multi-channel approach

Obviously, importance sampling of all propagators appearing in the amplitude is not possible by a single phase-space mapping. Therefore, we apply the *multi-channel approach* [20, 24] where N phase-space parametrizations with appropriate mappings, called *channels*, are used simultaneously. To this end, the phase-space integral is rewritten into the form

$$\int d\Phi^{2 \rightarrow 6} = \int_0^1 dr \sum_{i=1}^N \theta(r - \beta_{i-1}) \theta(\beta_i - r) \int_0^1 d^{14}\mathbf{r} \frac{1}{g_{\text{tot}}(\mathbf{r})}, \quad (3.9)$$

where the β_i define a partition of unity, i.e. $\beta_i = \sum_{j=1}^i \alpha_j$, $\beta_0 = 0$, $\beta_N = \sum_{j=1}^N \alpha_j = 1$. In Eq. (3.9) an additional random number r is introduced in order to select a *channel* i randomly with probability $\alpha_i \geq 0$. A channel is defined by its mapping from the pseudo-random numbers into the space of final-state momenta. The *total density* g_{tot} is composed of the single densities g_i of the different *channels* weighted by the *a priori weights* α_i :

$$g_{\text{tot}} = \sum_{i=1}^N \alpha_i g_i. \quad (3.10)$$

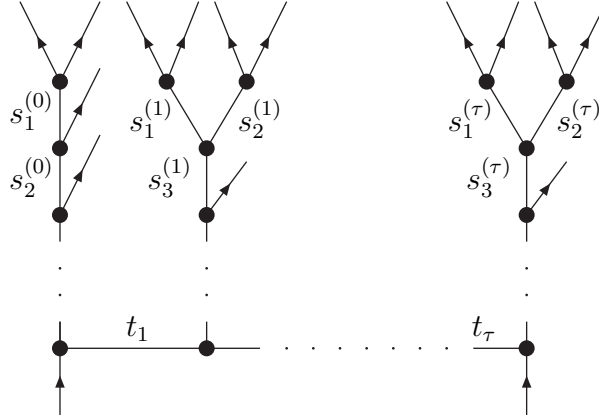


Figure 4: Topological diagram for the generic phase-space generator

In this way, it is possible to simultaneously include different phase-space mappings which are suitable for different parts of the integrand. To be specific, for each diagram a channel exists, so that all propagators of the squared diagram are smoothed by the corresponding local density g_i . No special channels are provided for interference contributions.

The a priori weights α_i are adapted in the early phase of the Monte Carlo run several times to optimize the convergence behaviour of the numerical integration. This *adaptive weight optimization* [25] increases the a priori weights α_i for such channels that correspond to important diagrams of the process, i.e. to diagrams that give large contributions to the total cross section.

The actual calculation is performed in two steps: First, a channel is chosen and the momenta of the final-state particles are calculated with the corresponding phase-space generator. Secondly, the total density is determined. Besides the evaluation of the matrix elements, the second step is the most time-consuming part since the local densities of all channels have to be calculated.

3.3 Generic construction of phase-space generators

Since six-fermion production processes involve of the order of 10^2 – 10^4 diagrams, it is very important to handle the different phase-space mappings in a generic way. All different channels can be obtained from one generic phase-space generator by choosing the topological structure of the corresponding diagram, as illustrated in Figure 4, the order of the incoming and outgoing particles, and the masses and widths of the internal particles. In contrast to the calculation of the matrix elements as discussed in Section 2, there is a fundamental difference between the incoming and outgoing particles, and s - and t -channel propagators.

For each class of diagrams with the same propagator structure we adopt an own channel for the numerical integration. Diagrams with four-particle vertices also fit into the generic diagram of Figure 4 if one of the propagators is contracted and the corresponding invariant is sampled uniformly. The same is true for diagrams with exclusively s -channel propagators, since the s -channel propagator resulting from a fusion of the two incoming lines is constant.

The actual calculation of the event kinematics is decomposed into three steps: the calculation of *time-like invariants*, of *2 → 2 scattering processes with t-channel propagators*, and of *1 → 2 particle decays*. The phase-space integration reads

$$\int d\Phi^{2 \rightarrow 6} = \prod_{i=1}^4 \int_{s_{i,\min}}^{s_{i,\max}} ds_i \prod_{j=1}^{\tau} \int d\Phi_j^{2 \rightarrow 2} \prod_{k=1}^{5-\tau} \int d\Phi_k^{1 \rightarrow 2}, \quad (3.11)$$

where the phase space of the 2 → 2 scattering processes and the 1 → 2 decays are denoted by $\Phi_j^{2 \rightarrow 2}$ and $\Phi_k^{1 \rightarrow 2}$, respectively. Note that the number τ of 2 → 2 scattering processes, which is the number of *t*-channel lines in Figure 4, can range from 0 to 5. The four invariants s_i ($i = 1, \dots, 4$) result from the phase-space factorization into scattering processes and decays. More details on phase-space parametrizations can be found in Refs. [35, 36]. If several *t*-channel propagators are present, i.e. for $\tau \geq 2$, some of the s_i ($i = 1, \dots, 4$) do not correspond to virtualities of propagators in the diagram; for such variables no mappings are introduced, they are generated uniformly.

In detail we proceed as follows:

(i) *Calculation of time-like invariants*

First of all, the time-like invariants $s_i^{(j)}$ are determined. The invariants corresponding to *s*-channel propagators are calculated from Eqs. (3.5)–(3.8). All other time-like invariants are sampled uniformly, i.e. calculated from Eq. (3.7) with $\nu = 0$. The determination of the invariants $s_i^{(j)}$ is ordered in such a way that the $s_i^{(j)}$ nearest to final-state particles are calculated first, followed by the next-to-nearest *s*-channel propagators, and so on.

The lower and upper limits $s_{i,\min/\max}^{(j)}$, in general, are functions of the already determined invariants. To enhance the efficiency of the numerical integration, separation cuts have to be taken into account. We include invariant-mass cuts of final-state particles in the evaluation of $s_{i,\min/\max}^{(j)}$ whenever possible.

(ii) *2 → 2 scattering processes with t-channel propagators*

The subpart of the diagram involving *t*-channel propagators is decomposed into several 2 → 2 scattering processes. The phase-space integration reads

$$\int d\Phi^{2 \rightarrow 2}(p_1, p_2; q_1, q_2) = \frac{1}{8\sqrt{(p_1 p_2)^2 - p_1^2 p_2^2}} \int_0^{2\pi} d\phi^* \int_{t_{\min}}^{t_{\max}} dt, \quad (3.12)$$

where $p_{1,2}$ are the incoming and $q_{1,2}$ are the outgoing momenta, and ϕ^* is the azimuthal angle defined by p_1 and q_1 in the CM frame of the subprocess, where $\mathbf{p}_1 + \mathbf{p}_2 = 0$. The argument $t = (p_1 - q_1)^2$ of the *t*-channel propagator is calculated according to Eqs. (3.5)–(3.8). The azimuthal angle ϕ^* is sampled uniformly. Since the corresponding polar angle $\cos \theta^*$ of this scattering process depends on the invariant t linearly,

$$t = \frac{p_1^2 q_2^2 + p_2^2 q_1^2 - 2(p_1 p_2)(q_1 q_2) + 2\sqrt{(p_1 p_2)^2 - p_1^2 p_2^2} \sqrt{(q_1 q_2)^2 - q_1^2 q_2^2} \cos \theta^*}{(p_1 + p_2)^2}, \quad (3.13)$$

the calculation of the momenta and the Lorentz transformation into the laboratory (LAB) frame is simple and, thus, skipped here. Explicit formulas can for instance be found in

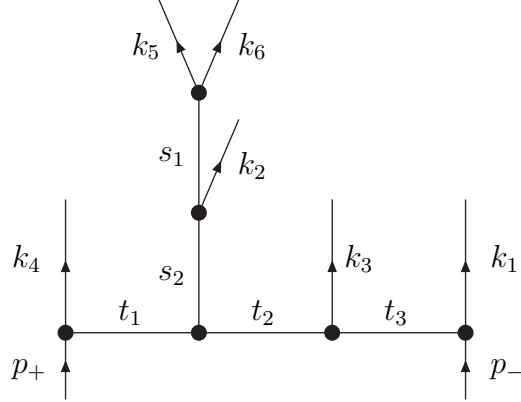


Figure 5: Topological diagram for a specific phase-space generator

Ref. [35]. Subprocesses that are nearest to the incoming particles of the whole $e^+e^- \rightarrow 6f$ scattering process are calculated first, followed by the next-to-nearest, and so on.

For the $2 \rightarrow 2$ scattering processes that are attached to the original incoming particles, we already take into account possible cuts on angles between outgoing particles and the beams that effectively reduce the integration range of t , i.e. we include these cuts in the determination of $t_{\min/\max}$.

(iii) $1 \rightarrow 2$ particle decays

It remains to perform the decays of the s -channel particles. The phase-space integration reads

$$\int d\Phi^{1 \rightarrow 2}(q_1, q_2) = \frac{\sqrt{(q_1 q_2)^2 - q_1^2 q_2^2}}{4(q_1 + q_2)^2} \int_0^{2\pi} d\phi^* \int_{-1}^1 d\cos\theta^*, \quad (3.14)$$

where ϕ^* and θ^* are the azimuthal and polar angles in the rest frame of the decaying particle, respectively. The variables ϕ^* and $\cos\theta^*$ are sampled uniformly. The momenta of the outgoing particles are q_1 and q_2 . As in the former step, the calculation of the momenta and the Lorentz transformation into the LAB frame is straightforward (see e.g. Ref. [35]).

We illustrate the general strategy by considering the specific topology shown in Figure 5, where a particular choice for the incoming and outgoing momenta p_{\pm} and k_i is made. For this example the phase-space parametrization (3.11) reads

$$\begin{aligned} \int d\Phi^{2 \rightarrow 6} \Big|_{\text{Fig.5}} &= \prod_{i=1}^4 \int_{s_{i,\min}}^{s_{i,\max}} ds_i \int d\Phi^{2 \rightarrow 2}(p_+, p_-; k_4, k_{12356}) \\ &\times \int d\Phi^{2 \rightarrow 2}(p_-, p_+ - k_4; k_1, k_{2356}) \int d\Phi^{2 \rightarrow 2}(p_+ - k_4, p_- - k_1; k_{256}, k_3) \\ &\times \int d\Phi^{1 \rightarrow 2}(k_2, k_{56}) \int d\Phi^{1 \rightarrow 2}(k_5, k_6), \end{aligned} \quad (3.15)$$

where sums of outgoing momenta are abbreviated by $k_{ij} = k_i + k_j$, $k_{ijk} = k_i + k_j + k_k$, etc. Note that only the time-like invariants $s_1 = k_{56}^2$ and $s_2 = k_{256}^2$ correspond to virtualities of propagators in the diagram, while $s_3 = k_{2356}^2$ and $s_4 = k_{12356}^2$ correspond to invariant masses of fictitious final-state particles within the first two $2 \rightarrow 2$ scattering processes.

For an efficient and fast numerical integration LUSIFER evaluates the different subparts of the phase-space mappings for all channels only once for a single event. The local densities of individual channels are then easily obtained from the Jacobians of these subparts. This speeds up the numerical integration considerably.

3.4 Cross checks

The Monte Carlo part of LUSIFER can, in principle, be applied to arbitrary processes. In order to check the phase-space integration, we implemented the tree-level matrix elements of RACOONWW, as given in Ref. [21], in LUSIFER and reproduced the results given in Table 1 of Ref. [21] for four-fermion production, $e^+e^- \rightarrow 4f$, and for the radiative processes, $e^+e^- \rightarrow 4f\gamma$, in the fixed width scheme. We found good agreement between the $4f$ and $4f\gamma$ results integrated with LUSIFER and RACOONWW.

4 Higher-order initial-state radiation at the leading logarithmic level

A first step to improve tree-level predictions by higher-order radiative corrections consists in including universal corrections such as the leading logarithms of initial-state radiation. In LUSIFER this is done via structure functions [26, 27]. The lowest-order differential cross section is convoluted in the energy fractions x_{\pm} of the incoming electron and positron:

$$\int d\sigma_{\text{Born+ISR}} = \int_0^1 dx_+ \Gamma_{ee}^{\text{LL}}(x_+, Q^2) \int_0^1 dx_- \Gamma_{ee}^{\text{LL}}(x_-, Q^2) \int d\sigma_{\text{Born}}(x_+p_+, x_-p_-), \quad (4.1)$$

where the splitting scale Q is not fixed at the leading logarithmic level and quantifies part of the missing radiative corrections. In LUSIFER, Q is set to the CM energy E_{CM} by default.³ The Born cross section in Eq. (4.1) is calculated in the same way as in the case without ISR but with the momenta $x_{\pm}p_{\pm}$ for the incoming e^{\pm} . The precise form of the structure function $\Gamma_{ee}^{\text{LL}}(x, Q^2)$ used in LUSIFER is the same as in Eqs. (5.2)–(5.4) of the second paper in Ref. [22].

5 Classification of $6f$ final states in e^+e^- collisions

The derivation of squared matrix elements described in Section 2 is valid for all processes involving eight external fermions and restricted for gluonic diagrams to processes involving up to four external quarks. Thus, these results can be applied to various six-fermion processes in lepton–lepton, lepton–hadron, and hadron–hadron scattering. In this paper, we focus on $e^+e^- \rightarrow 6f$ processes in the following, representing an important class of reactions at future linear colliders such as TESLA [1]. We divide the set of $6f$ final states into three (overlapping) subsets corresponding to different subprocesses of interest:

³For scattering processes that are dominated by small splitting scales the use of purely s -dependent structure functions is not a good approximation for treating ISR effects. This is, in particular, the case if e^{\pm} are scattered in the very forward direction. Possible improvements for such situations have been, for instance, described in the context of single-W production in $e^+e^- \rightarrow 4f$ (see e.g. Refs. [2, 37]).

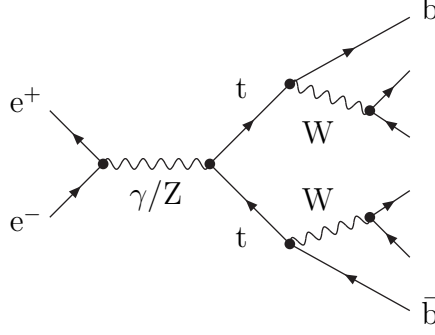


Figure 6: Diagram for $t\bar{t}$ production: $e^+e^- \rightarrow t\bar{t} \rightarrow bW^+\bar{b}W^- \rightarrow 6f$

(i) *Processes involving top quarks*

The most interesting processes involving top quarks correspond to top-pair production with the subsequent decay of the top quarks into six fermions which proceeds via W bosons, $e^+e^- \rightarrow t\bar{t} \rightarrow bW^+\bar{b}W^- \rightarrow 6f$. The corresponding diagram is shown in Figure 6. All $6f$ final states that are relevant for $t\bar{t}$ production are of the form $e^+e^- \rightarrow b\bar{b}f_1\bar{f}_1'f_2\bar{f}_2'$, where $f_i\bar{f}_i'$ ($i = 1, 2$) are two weak isospin doublets.

There is a second, but less interesting class of $6f$ final states that involve top-quark diagrams but do not contain $t\bar{t}$ production as a subprocess. These processes are of the form $e^+e^- \rightarrow \nu_e\bar{\nu}_e b\bar{b}f\bar{f}$, where f is any fermion other than the electron.

(ii) *Vector-boson scattering and s-channel Higgs production*

One of the most interesting class of subprocesses in $e^+e^- \rightarrow 6f$ is the scattering of weak gauge bosons, $e^+e^- \rightarrow 2f + (V_1V_2 \rightarrow V_3V_4) \rightarrow 6f$. According to the charges of the “incoming” vector-boson pair V_1V_2 , there are three different types of vector-boson scattering channels, as shown in Figure 7: (a) neutral–neutral, (b) charged–charged, and (c) mixed. Among all $6f$ final states these channels are distinguished by the appearance of (a) e^+e^- , (b) $\nu_e\bar{\nu}_e$, and (c) $e^+\nu_e/e^-\bar{\nu}_e$ in the final state.

ZZ and WW fusion processes, which are included in types (a) and (b), are also important in Higgs physics. If the Higgs-boson mass M_H is large enough that the decay channel $H \rightarrow WW$ opens, resonant s-channel Higgs production dominates the vector-boson scattering cross section, $WW, ZZ \rightarrow H \rightarrow WW/ZZ$, which is then one of the two main production mechanisms for the Higgs boson in e^+e^- annihilation. The relevant Feynman diagram is shown in Figure 7(d).

(iii) *Three-boson production and Higgs-strahlung off Z bosons*

All $6f$ final states have in common that they contribute to production processes of three electroweak gauge bosons, $e^+e^- \rightarrow V_1V_2V_3 \rightarrow 6f$. As illustrated in Figure 8, there are two different types of reactions, distinguished by the charges of the produced bosons: (a) charged–charged–neutral and (b) neutral–neutral–neutral.

For a sufficiently large Higgs-boson mass, i.e. when $H \rightarrow WW$ becomes possible, not only s-channel Higgs production leads to relatively large contributions to $6f$ production but also Higgs-strahlung off Z bosons, $e^+e^- \rightarrow ZH \rightarrow ZWW/ZZZ \rightarrow 6f$, which is the second of the two main Higgs production mechanisms at future e^+e^- colliders. The corresponding Feynman diagram is shown in Figure 8(c).

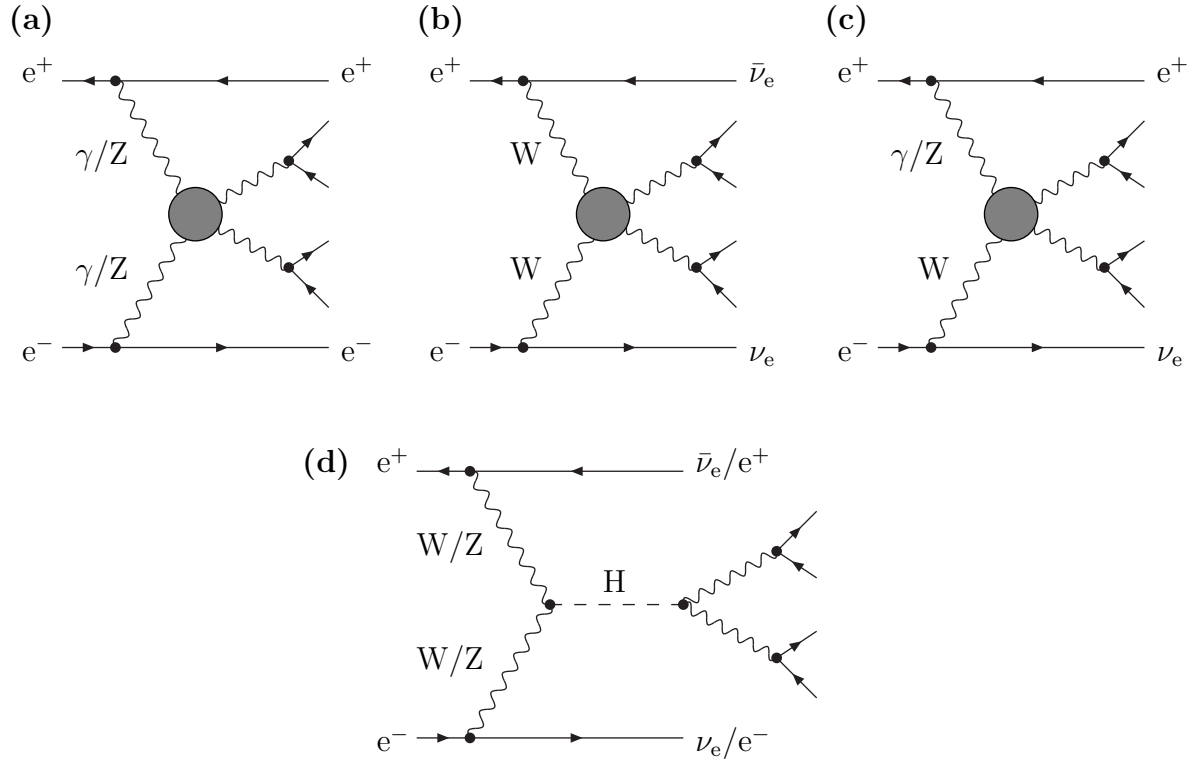


Figure 7: Diagram structures for vector-boson scattering: $e^+e^- \rightarrow 2f + (V_1V_2 \rightarrow V_3V_4) \rightarrow 6f$

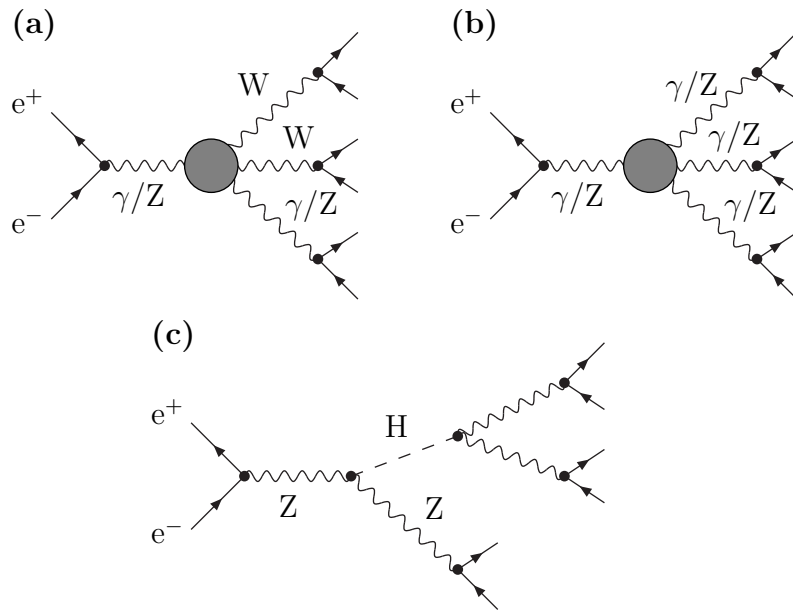


Figure 8: Diagram structures for three-boson production: $e^+e^- \rightarrow V_1V_2V_3 \rightarrow 6f$

6 Numerical results

6.1 Input parameters

For the numerical evaluation we use the following set of Standard-Model parameters [38],

$$\begin{aligned}
G_\mu &= 1.16639 \times 10^{-5} \text{ GeV}^{-2}, & \alpha(0) &= 1/137.0359895, \\
\alpha_s(M_Z) &= 0.1181, \\
M_W &= 80.419 \text{ GeV}, & \Gamma_W &= 2.12 \text{ GeV}, \\
M_Z &= 91.1882 \text{ GeV}, & \Gamma_Z &= 2.4952 \text{ GeV}, \\
m_t &= 174.3 \text{ GeV}, & \Gamma_t &= 1.6 \text{ GeV}, \\
m_e &= 0.51099907 \text{ MeV},
\end{aligned} \tag{6.1}$$

where the top-quark width Γ_t is, of course, only a reasonable estimate. In order to absorb parts of the renormalization effects (i.e. some universal radiative corrections) into the electroweak couplings, such as the running of $\alpha(Q^2)$ from $Q^2 = 0$ to a high-energy scale and some universal effects related to the ρ parameter, we evaluate amplitudes in the so-called G_μ scheme, i.e. we derive the electromagnetic coupling $\alpha = e^2/(4\pi)$ from the Fermi constant G_μ according to

$$\alpha_{G_\mu} = \frac{\sqrt{2}G_\mu M_W^2 s_w^2}{\pi}. \tag{6.2}$$

In the structure functions we use $\alpha(0)$ as coupling parameter, which is the correct effective coupling for real photon emission. For the Higgs-boson mass we take the set of sample values listed in Table 2, including also the corresponding Higgs-boson widths, which are calculated with the program HDECAY [39]. If not stated otherwise, we take the value $M_H = 170 \text{ GeV}$ by default.

$M_H [\text{GeV}]$	170	190	230
$\Gamma_H [\text{GeV}]$	0.3835	1.038	2.813

Table 2: Higgs-boson masses and decay widths as provided by HDECAY

With the only exception of Section 6.5, where the interplay between finite-width schemes and gauge invariance is discussed, we make use of the fixed-width approach, as described in Section 2.3.

Finally, we specify the following separation cuts:

$$\begin{aligned}
\theta(l, \text{beam}) &> 5^\circ, & \theta(q, \text{beam}) &> 5^\circ, & \theta(l, l') &> 5^\circ, & \theta(l, q) &> 5^\circ, \\
E_l &> 10 \text{ GeV}, & E_q &> 10 \text{ GeV}, & m(q, q') &> 10 \text{ GeV},
\end{aligned} \tag{6.3}$$

where $\theta(i, j)$ is the angle between the particles i and j in the LAB system, and l , q , and “beam” denote charged final-state leptons, quarks, and the beam electrons or positrons, respectively. The invariant mass of a quark pair qq' is denoted by $m(q, q')$.

6.2 Survey of cross sections

Only very few results presented in the literature are found to be appropriate for a tuned comparison to our results, because in most cases only plots but no numbers are given, fermion mass singularities are not always excluded by phase-space cuts, or beamstrahlung effects are included. Therefore, we decided to adopt a public version of a multi-purpose generator available from the `www` and to perform a tuned comparison based on the setup described in the previous section as far as possible. Specifically, we have used the generator WHIZARD [14], version 1.21, together with the implemented MADGRAPH [28] amplitudes. We did not include beamstrahlung effects in the following results, since they depend on the details of the inspected collider and would spoil the usefulness of our results as reference for future studies. Beamstrahlung can, however, be included in LUSIFER in a straightforward way. If not stated otherwise the cross section numbers in this section are based on 10^7 weighted Monte Carlo events. In the following tables, the numbers within parentheses correspond to the statistical errors of the Monte Carlo integrations.

In Table 3 we show the results for all processes $e^+e^- \rightarrow 6 \text{ leptons}$ with up to two neutrinos in the final state (three neutrinos are not possible) for a CM energy of 500 GeV. The first set of final states comprises the reactions that receive contributions from resonant WWZ production and various other mechanisms. The remaining reactions entirely proceed via neutral-current interactions, except for the last two processes that receive contributions from $WW \rightarrow ZZ$ scattering. Comparing the two sets of cross sections, the ones for WWZ production are larger. ISR affects the cross sections at the level of a few per cent, ranging up to $\sim 8\%$, and this correction is negative in almost all cases. The comparison with WHIZARD and MADGRAPH reveals agreement within $1\text{--}3\sigma$ in general with a few exceptions, where larger differences occur. These differences are accompanied with larger errors in the WHIZARD results and are assumed [40] to be due to the fact that the photon propagators in the splittings $\gamma \rightarrow f\bar{f}$ are not analytically smoothed by mappings in WHIZARD. In most cases the statistical error given by LUSIFER is smaller than the one of WHIZARD. The missing entries correspond to those final states that are not supported by MADGRAPH.⁴

Table 4 shows a tuned comparison for $6f$ final states containing two quarks and at most three neutrinos for a CM energy of 500 GeV. The table is divided into two parts: the first part comprises all final states that receive contributions from a hadronically decaying W boson; final states corresponding to hadronically decaying Z bosons form the second part, where contributions from $u\bar{u}$ and $d\bar{d}$ pairs are added, in order to keep the table more compact. In comparison with the purely leptonic final states the cross sections are larger, which is mainly due to the colour factor 3 resulting from the two quarks in the final states. Otherwise the various channels show similar features as their leptonic counterparts. WWZ production channels have larger cross sections than processes that proceed via neutral-current interactions only, and ISR affects cross sections at the level of a few per cent, mainly in negative direction. It should be mentioned that in the second set of final states the LUSIFER results have again been obtained from 10^7 events, while the WHIZARD runs have been performed with 10^7 events for $u\bar{u}$ and $d\bar{d}$ each, so that the final

⁴In contrast to the MADGRAPH version used for checking the amplitudes, as described in Section 2.4, the MADGRAPH version within WHIZARD is neither able to add electroweak and gluon-exchange diagrams coherently, nor to deal with more than 999 Feynman graphs for a given process.

$e^+e^- \rightarrow$	LUSIFER		WHIZARD & MADGRAPH	
	$\sigma_{\text{Born}}[\text{fb}]$	$\sigma_{\text{Born+ISR}}[\text{fb}]$	$\sigma_{\text{Born}}[\text{fb}]$	$\sigma_{\text{Born+ISR}}[\text{fb}]$
$\mu^- \mu^+ \mu^- \mu^+ \nu_\mu \bar{\nu}_\mu$	0.041382(87)	0.040883(81)	0.04130(19)	0.04077(27)
$\mu^- \mu^+ \mu^- \bar{\nu}_\mu \nu_\tau \tau^+$	0.040320(80)	0.04002(12)	0.04044(19)	0.03961(15)
$\mu^- \mu^+ \nu_\mu \bar{\nu}_\mu \tau^- \tau^+$	0.042297(84)	0.041966(89)	0.04212(12)	0.04165(33)
$e^- \bar{\nu}_e \mu^- \mu^+ \nu_\mu \mu^+$	0.04729(10)	0.04640(12)	0.04713(25)	0.04549(20)
$e^- \bar{\nu}_e \mu^- \mu^+ \nu_\tau \tau^+$	0.04708(14)	0.04629(14)	0.04705(16)	0.04702(62)
$e^- e^+ \nu_e \bar{\nu}_e \mu^- \mu^+$	0.06309(20)	0.06026(18)	0.06139(26)	0.05980(65)
$e^- e^+ \mu^- \mu^+ \nu_\mu \bar{\nu}_\mu$	0.18300(36)	0.16838(32)	0.18302(32)	0.16976(36)
$e^- e^+ \mu^- \bar{\nu}_\mu \nu_\tau \tau^+$	0.18023(21)	0.16555(30)	0.18101(31)	0.16661(43)
$e^- e^+ e^- \bar{\nu}_e \nu_\mu \mu^+$	0.18603(25)	0.17091(41)	0.18624(39)	0.17118(48)
$e^- e^+ e^- e^+ \nu_e \bar{\nu}_e$	0.19702(36)	0.18065(35)	–	–
$\mu^- \mu^+ \mu^- \mu^+ \mu^- \mu^+$	0.00026849(54)	0.00027067(57)	–	–
$\mu^- \mu^+ \mu^- \mu^+ \tau^- \tau^+$	0.0008088(15)	0.0008182(16)	0.0007925(69)	0.0007689(79)
$e^- e^+ \mu^- \mu^+ \mu^- \mu^+$	0.002514(16)	0.002437(16)	0.00211(18)	0.001467(78)
$e^- e^+ \mu^- \mu^+ \tau^- \tau^+$	0.005102(31)	0.005005(37)	0.00445(16)	0.00464(23)
$e^- e^+ e^- e^+ \mu^- \mu^+$	0.004158(31)	0.004017(39)	–	–
$e^- e^+ e^- e^+ e^- e^+$	0.001803(16)	0.001758(15)	–	–
$\mu^- \mu^+ \mu^- \mu^+ \nu_\tau \bar{\nu}_\tau$	0.0010312(16)	0.0010262(16)	0.0010295(36)	0.0010257(43)
$e^- e^+ \mu^- \mu^+ \nu_\tau \bar{\nu}_\tau$	0.0033141(69)	0.0031918(72)	0.003296(14)	0.003133(23)
$e^- e^+ e^- e^+ \nu_\mu \bar{\nu}_\mu$	0.0022162(60)	0.0020908(62)	–	–
$\nu_e \bar{\nu}_e \mu^- \mu^+ \mu^- \mu^+$	0.003730(14)	0.0034166(76)	0.003613(25)	0.003374(34)
$\nu_e \bar{\nu}_e \mu^- \mu^+ \tau^- \tau^+$	0.007366(17)	0.006785(16)	0.007301(33)	0.006503(67)

Table 3: Cross sections for $e^+e^- \rightarrow 6f$ channels with purely leptonic final states for $\sqrt{s} = 500 \text{ GeV}$

numbers effectively result from 2×10^7 events. In view of this difference the statistical error of LUSIFER is somewhat smaller. The agreement between the two programs is again within $1\text{--}3\sigma$ with a few exceptions for the same reason as explained above.

A tuned comparison of results for final states containing two leptons and four quarks is presented in Table 5, again for a CM energy of 500 GeV. The notation “4q” stands for the sum over all possible four-quark configurations of u, d, c, s quarks. In the table we separately give results that include or exclude the contributions of gluon-exchange diagrams in the amplitude calculation, as indicated in the “QCD” column. Note that the large impact of these gluon-exchange diagrams sensitively depends on the separation cuts, in particular on the minimal invariant mass of quark pairs. The impact of ISR is similar to the cases discussed previously. The largest cross section is observed for $\nu_e \bar{\nu}_e + 4q$ production, which is the only channel that receives contributions from $WW \rightarrow WW/\text{ZZ}$ scattering and from W fusion to a Higgs boson. The comparison to WHIZARD shows the

$e^+e^- \rightarrow$	LUSIFER		WHIZARD & MADGRAPH	
	$\sigma_{\text{Born}}[\text{fb}]$	$\sigma_{\text{Born+ISR}}[\text{fb}]$	$\sigma_{\text{Born}}[\text{fb}]$	$\sigma_{\text{Born+ISR}}[\text{fb}]$
$\mu^- \mu^+ \mu^- \bar{\nu}_\mu u \bar{d}$	0.11835(22)	0.11714(22)	0.11797(26)	0.11732(71)
$\mu^- \mu^+ \tau^- \bar{\nu}_\tau u \bar{d}$	0.11861(42)	0.11695(22)	0.11791(21)	0.11664(29)
$e^- \bar{\nu}_e \mu^- \mu^+ u \bar{d}$	0.13832(30)	0.13516(34)	0.13785(36)	0.13510(62)
$e^- e^+ \mu^- \bar{\nu}_\mu u \bar{d}$	0.53352(70)	0.48897(69)	0.53493(61)	0.49378(73)
$e^- e^+ e^- \bar{\nu}_e u \bar{d}$	0.55089(74)	0.50464(72)	0.5514(13)	0.5061(10)
$\mu^- \bar{\nu}_\mu \nu_\mu \bar{\nu}_\mu u \bar{d}$	0.18399(11)	0.18182(11)	0.18396(13)	0.18204(14)
$\mu^- \bar{\nu}_\mu \nu_\tau \bar{\nu}_\tau u \bar{d}$	0.18406(10)	0.18201(11)	0.18430(13)	0.18197(14)
$e^- \bar{\nu}_e \nu_\mu \bar{\nu}_\mu u \bar{d}$	0.20272(14)	0.19847(14)	0.20288(14)	0.19843(16)
$\nu_e \bar{\nu}_e \mu^- \bar{\nu}_\mu u \bar{d}$	1.6326(12)	1.4743(12)	1.6313(13)	1.4746(13)
$e^- \bar{\nu}_e \nu_e \bar{\nu}_e u \bar{d}$	1.6500(17)	1.4906(15)	1.6482(15)	1.4914(14)
$\mu^- \mu^+ \nu_\mu \bar{\nu}_\mu (u\bar{u}+d\bar{d})$	0.26632(36)	0.26266(33)	0.26647(19)	0.26242(21)
$\mu^- \bar{\nu}_\mu \nu_\tau \tau^+ (u\bar{u}+d\bar{d})$	0.25408(18)	0.25068(19)	0.25427(17)	0.25067(17)
$e^- \bar{\nu}_e \nu_\mu \mu^+ (u\bar{u}+d\bar{d})$	0.28161(24)	0.27514(24)	0.28189(21)	0.27471(21)
$e^- e^+ \nu_e \bar{\nu}_e (u\bar{u}+d\bar{d})$	0.35788(62)	0.34361(73)	0.35917(62)	0.34366(36)
$\mu^- \mu^+ \mu^- \mu^+ (u\bar{u}+d\bar{d})$	0.0043727(73)	0.0043774(77)	0.004368(18)	0.004303(18)
$\mu^- \mu^+ \tau^- \tau^+ (u\bar{u}+d\bar{d})$	0.008731(14)	0.008736(15)	0.008652(26)	0.008585(41)
$e^- e^+ \mu^- \mu^+ (u\bar{u}+d\bar{d})$	0.015466(59)	0.014886(49)	0.01523(11)	0.01396(27)
$e^- e^+ e^- e^+ (u\bar{u}+d\bar{d})$	0.010730(58)	0.010207(45)	–	–
$\mu^- \mu^+ \nu_\tau \bar{\nu}_\tau (u\bar{u}+d\bar{d})$	0.012057(17)	0.012021(17)	0.012042(12)	0.011964(19)
$e^- e^+ \nu_\mu \bar{\nu}_\mu (u\bar{u}+d\bar{d})$	0.016967(30)	0.016484(32)	0.017006(23)	0.016417(25)
$\nu_e \bar{\nu}_e \mu^- \mu^+ (u\bar{u}+d\bar{d})$	0.044940(85)	0.041135(86)	0.044976(64)	0.04083(11)

Table 4: Cross sections for $e^+e^- \rightarrow 6f$ channels with four leptons and two quarks in the final state for $\sqrt{s} = 500 \text{ GeV}$

same features as in the other cases. However, it should be mentioned that all $4q$ final states have been integrated individually with WHIZARD, but in a single run with LUSIFER. This explains the smaller integration errors of the WHIZARD results. Since the MADGRAPH version included in WHIZARD is not able to coherently add gluon-exchange and purely electroweak diagrams, a comparison of cross sections based on the full amplitudes has not been carried out.

Finally, in Table 6 we collect our results on cross sections for final states that involve amplitudes with intermediate top quarks. The first set of channels comprises all final states that are relevant for top-quark pair production, $e^+e^- \rightarrow t\bar{t} \rightarrow 6f$. In the second set of processes top quarks appear only on non-resonant lines in diagrams. The difference between the $t\bar{t}$ production cross sections for two and four quarks in the final states roughly reflects the factor 3 between leptonically and hadronically decaying W bosons that have been produced in $t \rightarrow bW^+$. Since these channels are strongly dominated by the diagram

$e^+e^- \rightarrow$	QCD?	LUSIFER		WHIZARD & MADGRAPH	
		$\sigma_{\text{Born}}[\text{fb}]$	$\sigma_{\text{Born+ISR}}[\text{fb}]$	$\sigma_{\text{Born}}[\text{fb}]$	$\sigma_{\text{Born+ISR}}[\text{fb}]$
$\mu^- \bar{\nu}_\mu + 4q$	yes	3.8170(84)	3.7917(86)	–	–
	no	2.9603(28)	2.9172(27)	2.9616(13)	2.9195(13)
$e^- \bar{\nu}_e + 4q$	yes	4.605(13)	4.529(14)	–	–
	no	3.2798(38)	3.1930(40)	3.2708(16)	3.1916(17)
$\mu^- \mu^+ + 4q$	yes	1.5150(30)	1.5017(31)	–	–
	no	1.4406(40)	1.4227(29)	1.4343(18)	1.4192(19)
$\nu_\mu \bar{\nu}_\mu + 4q$	yes	2.3405(29)	2.3147(28)	–	–
	no	2.2466(33)	2.2138(26)	2.2440(12)	2.2153(13)
$e^- e^+ + 4q$	yes	6.570(17)	6.053(16)	–	–
	no	6.1439(95)	5.679(10)	6.2001(50)	5.7115(60)
$\nu_e \bar{\nu}_e + 4q$	yes	19.260(40)	17.441(37)	–	–
	no	18.850(32)	17.038(29)	18.879(11)	17.076(11)

Table 5: Cross sections for $e^+e^- \rightarrow 6f$ channels with two leptons and four quarks in the final state for $\sqrt{s} = 500 \text{ GeV}$

$e^+e^- \rightarrow$	QCD?	LUSIFER		WHIZARD & MADGRAPH	
		$\sigma_{\text{Born}}[\text{fb}]$	$\sigma_{\text{Born+ISR}}[\text{fb}]$	$\sigma_{\text{Born}}[\text{fb}]$	$\sigma_{\text{Born+ISR}}[\text{fb}]$
$\mu^- \bar{\nu}_\mu \nu_\mu \mu^+ b \bar{b}$	–	5.8091(49)	5.5887(36)	5.8102(26)	5.5978(30)
$\mu^- \bar{\nu}_\mu \nu_\tau \tau^+ b \bar{b}$	–	5.7998(36)	5.5840(40)	5.7962(26)	5.5893(29)
$e^- \bar{\nu}_e \nu_\mu \mu^+ b \bar{b}$	–	5.8188(45)	5.6042(38)	5.8266(27)	5.6071(30)
$e^- \bar{\nu}_e \nu_e e^+ b \bar{b}$	–	5.8530(68)	5.6465(70)	5.8751(30)	5.6508(36)
$\mu^- \bar{\nu}_\mu u \bar{d} b \bar{b}$	yes	17.171(24)	16.561(24)	–	–
	no	17.095(11)	16.4538(98)	17.1025(80)	16.4627(87)
$e^- \bar{\nu}_e u \bar{d} b \bar{b}$	yes	17.276(45)	16.577(21)	–	–
	no	17.187(21)	16.511(12)	17.1480(82)	16.5288(92)
$\nu_e \bar{\nu}_e \mu^- \mu^+ b \bar{b}$		0.024550(45)	0.022472(45)	0.024619(43)	0.022398(41)
$\nu_e \bar{\nu}_e u \bar{u} b \bar{b}$	yes	0.12625(32)	0.11703(32)	–	–
	no	0.06984(15)	0.06369(14)	0.069781(70)	0.063635(86)
$\nu_e \bar{\nu}_e d \bar{d} b \bar{b}$	yes	0.13709(41)	0.12636(37)	–	–
	no	0.08648(20)	0.07871(18)	0.086351(83)	0.078533(96)
$\nu_e \bar{\nu}_e b \bar{b} b \bar{b}$	yes	0.06741(18)	0.06226(18)	–	–
	no	0.04352(10)	0.03974(12)	0.043473(49)	0.039721(68)

Table 6: Cross sections for $e^+e^- \rightarrow 6f$ channels involving intermediate top quarks for $\sqrt{s} = 500 \text{ GeV}$

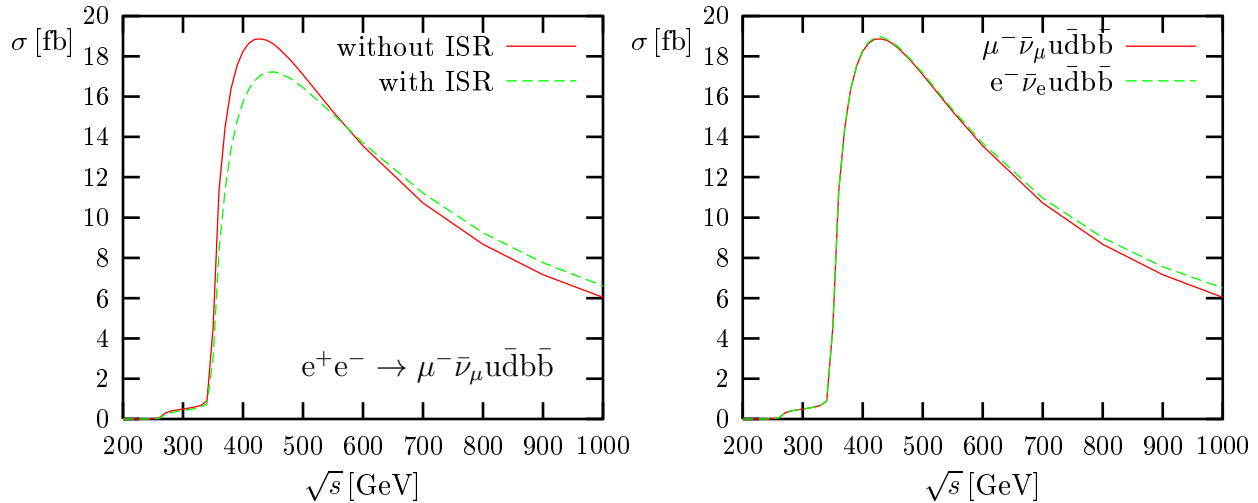


Figure 9: Total cross section of $e^+e^- \rightarrow \mu^-\bar{\nu}_\mu u\bar{d}b\bar{b}$ (without gluon-exchange diagrams) as function of the CM energy with and without ISR on the l.h.s. and in comparison with $e^+e^- \rightarrow e^-\bar{\nu}_e u\bar{d}b\bar{b}$ (without ISR) on the r.h.s.

shown in Figure 6, the impact of gluon-exchange diagrams is small. Concerning the ISR effects and the comparison of the two programs, the same features are observed as in the other cases discussed above.

Finally, we mention that LUSIFER runs faster than the combination of the WHIZARD and MADGRAPH packages. The factor in speed varies with the $6f$ final state from roughly a factor of 2 up to an order of magnitude, where the superiority of LUSIFER becomes more apparent if a large number of diagrams is involved.

6.3 Results on top-quark pair production

Figure 9 illustrates the (well-known) energy dependence of the top-quark pair production cross section for final states where one of the produced W bosons decays hadronically and the other leptonically. The results for the total cross section are obtained with 5×10^6 events per CM energy. Gluon-exchange diagrams are not taken into account. The cross section steeply rises at the $t\bar{t}$ threshold, reaches its maximum between 400 GeV and 500 GeV, and then decreases with increasing energy. The l.h.s. of the figure shows that ISR reduces the cross section for energies below its maximum and enhances it above, thereby shifting the maximum to a higher energy. This behaviour is simply due to the radiative energy loss induced by ISR. Near a CM energy of 250 GeV the onset of WWZ production can be observed. Note that this contribution is entirely furnished by background diagrams, i.e. by diagrams that do not have a resonant top-quark pair. Another type of background diagrams exists if electrons or positrons are present in the final state, since an incoming e^\pm line can then go through to the final state. The impact of such diagrams is illustrated on the r.h.s. of Figure 9, where the final states are equal up to the change of $\mu^-\bar{\nu}_\mu$ to $e^-\bar{\nu}_e$. For energies around 500 GeV the difference is of the order of a per cent, but increasing with energy. It should, however, be noted that this difference strongly depends on the separation of final-state e^\pm from the beams. For smaller cut

angles, or for particular regions in distributions, the impact of such background diagrams will be much larger.⁵ The problem of working out an optimal strategy to define a clear $t\bar{t}$ signal, i.e. to systematically suppress background contributions, obviously goes beyond this study.

In Figures 10 and 11 we consider two examples of distributions that are interesting for $t\bar{t}$ production, again focusing on the channel $e^+e^- \rightarrow \mu^- \bar{\nu}_\mu u \bar{d} b \bar{b}$. Figure 10 shows the invariant-mass distribution of the $u\bar{d}b$ quark triple that results from the top-quark decay. As expected, ISR does not distort the resonance shape but merely rescales the Breit–Wigner-like distribution. More interestingly, the r.h.s. of the figure demonstrates that LUSIFER and WHIZARD yield predictions that are fully compatible within statistical accuracy, both with and without the inclusion of ISR corrections. Figure 11 shows the production angular distribution of the $u\bar{d}b$ quark triple, which is (for resonant top quarks) equal to the top-quark production angle. ISR tends to flatten the distribution, which is again due to the impact of effectively reduced scattering energies where the distribution is less angular dependent. The r.h.s. of the figure reveals agreement between the two programs within statistical errors.

6.4 Results on Higgs-boson production

In this section we discuss some distributions that are relevant for Higgs-boson production in the intermediate M_H range. Figures 12 and 13 show the four-quark invariant-mass distribution and the related production angular distribution of the individual channel $e^+e^- \rightarrow \nu_\mu \bar{\nu}_\mu u \bar{d} s \bar{c}$ for a CM energy of 500 GeV. Gluon-exchange diagrams are not included in these evaluations. The reaction is dominated by two mechanisms: ZH production with the subsequent decays $H \rightarrow WW \rightarrow 4q$ and $Z \rightarrow \nu_\mu \bar{\nu}_\mu$, and “continuous” WWZ production. In the invariant-mass distribution the narrow Higgs resonance shows up at $M_{u\bar{d}s\bar{c}} = M_H = 170$ GeV over a continuous background from WWZ production in the range $2M_W \lesssim M_{u\bar{d}s\bar{c}} \lesssim \sqrt{s} - M_Z$. The l.h.s. of Figure 12 shows that ISR does not influence the resonance structure strongly; the largest ISR effect is observed at the upper edge of the spectrum, where the effective CM energy loss by ISR reduces the rate. The r.h.s. of the figure illustrates the agreement between the LUSIFER and WHIZARD results within statistical accuracy. Figure 13 shows that ISR significantly distorts the four-quark angular distribution at intermediate angles, where ZH production dominates; in the very forward and backward regions the spectrum is mainly due to contributions from the subprocess $e^+e^- \rightarrow (\gamma^*/Z^*)Z \rightarrow WWZ$, where the total momentum of the $u\bar{d}s\bar{c}$ quark system correspond to the off-shell particles γ^*/Z^* . The r.h.s. of the figure again demonstrates the good agreement between the two different Monte Carlo programs.

In Figure 14 we show the analogous distributions for three different Higgs-boson masses, but now summed over all four-quark configurations of the first two generations. Figure 15 shows the same distributions after replacing the $\nu_\mu \bar{\nu}_\mu$ pair in the final state by $\nu_e \bar{\nu}_e$. ISR and gluon-exchange diagrams are not included in these evaluations. The crucial difference between the $\nu_\mu \bar{\nu}_\mu$ and $\nu_e \bar{\nu}_e$ channels lies in the Higgs production mechanisms: while the former receives only contributions from ZH production, the latter additionally involves W fusion, $WW \rightarrow H \rightarrow WW$, which dominates the cross section. Therefore,

⁵These features are well-known from $4f$ physics, where forward-scattered e^\pm , in particular, are used to define the so-called single-W production signal (see, e.g., Ref. [2, 37]).

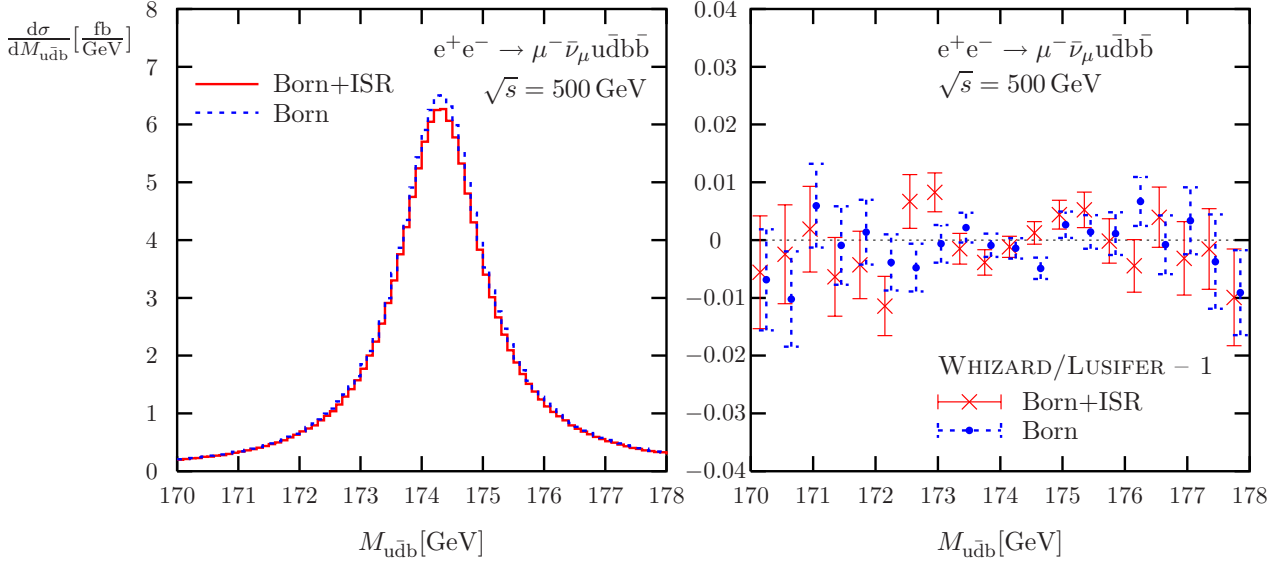


Figure 10: Invariant-mass distribution of the $u\bar{d}b$ quark triple in $e^+e^- \rightarrow \mu^- \bar{\nu}_\mu u\bar{d}b\bar{b}$ (without gluon-exchange diagrams): absolute prediction with and without ISR (l.h.s.) and comparison between LUSIFER and WHIZARD (r.h.s.)

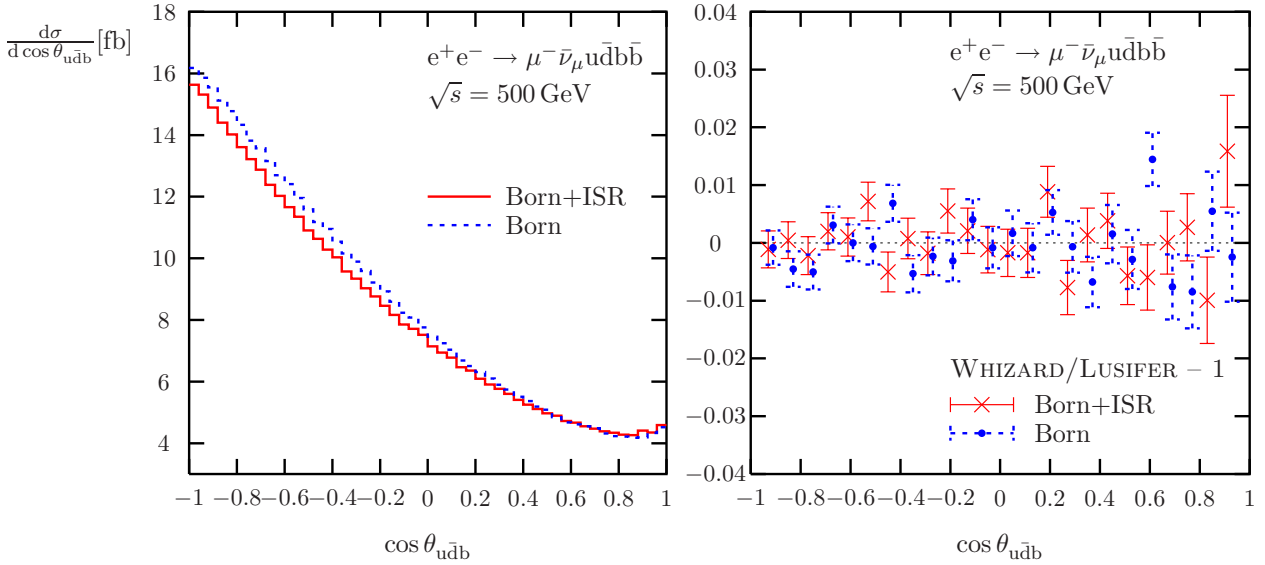


Figure 11: Angular distribution of the $u\bar{d}b$ quark triple in $e^+e^- \rightarrow \mu^- \bar{\nu}_\mu u\bar{d}b\bar{b}$ (without gluon-exchange diagrams): absolute prediction with and without ISR (l.h.s.) and comparison between LUSIFER and WHIZARD (r.h.s.)

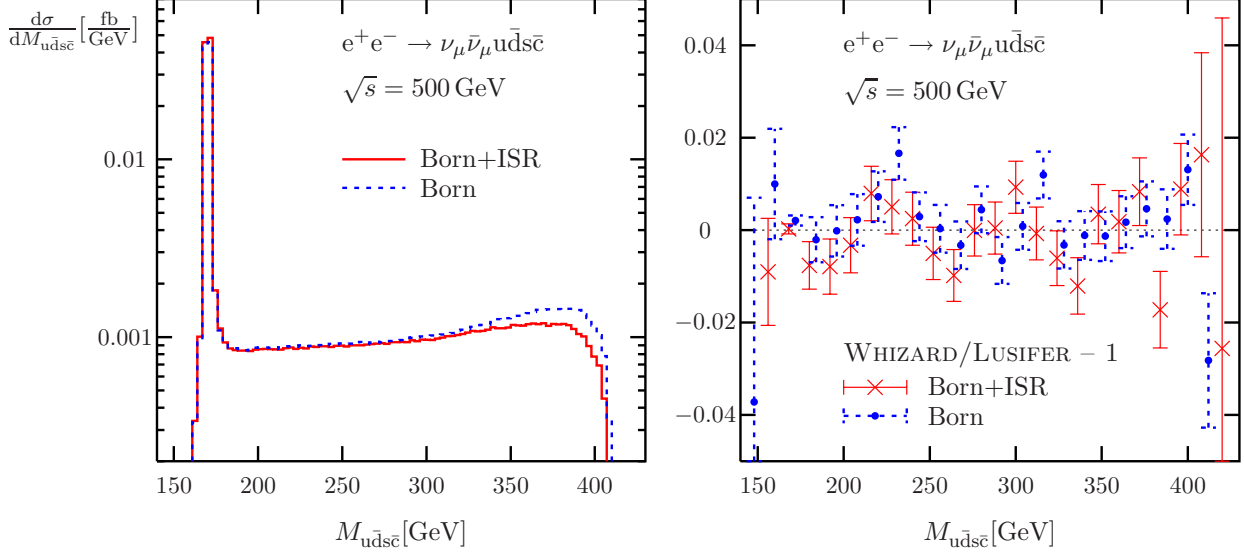


Figure 12: Invariant-mass distribution of the $u\bar{d}s\bar{c}$ quark system in $e^+e^- \rightarrow \nu_\mu \bar{\nu}_\mu u\bar{d}s\bar{c}$ (without gluon-exchange diagrams): absolute prediction with and without ISR (l.h.s.) and comparison between LUSIFER and WHIZARD (r.h.s.)

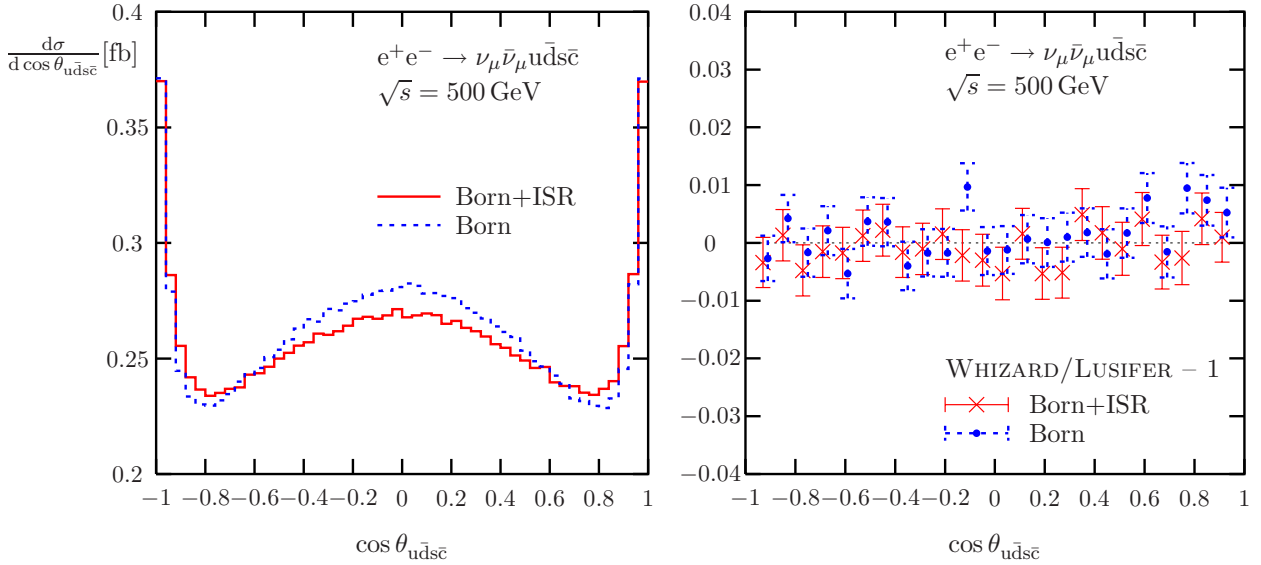


Figure 13: Angular distribution of the $u\bar{d}s\bar{c}$ quark system in $e^+e^- \rightarrow \nu_\mu \bar{\nu}_\mu u\bar{d}s\bar{c}$ (without gluon-exchange diagrams): absolute prediction with and without ISR (l.h.s.) and comparison between LUSIFER and WHIZARD (r.h.s.)

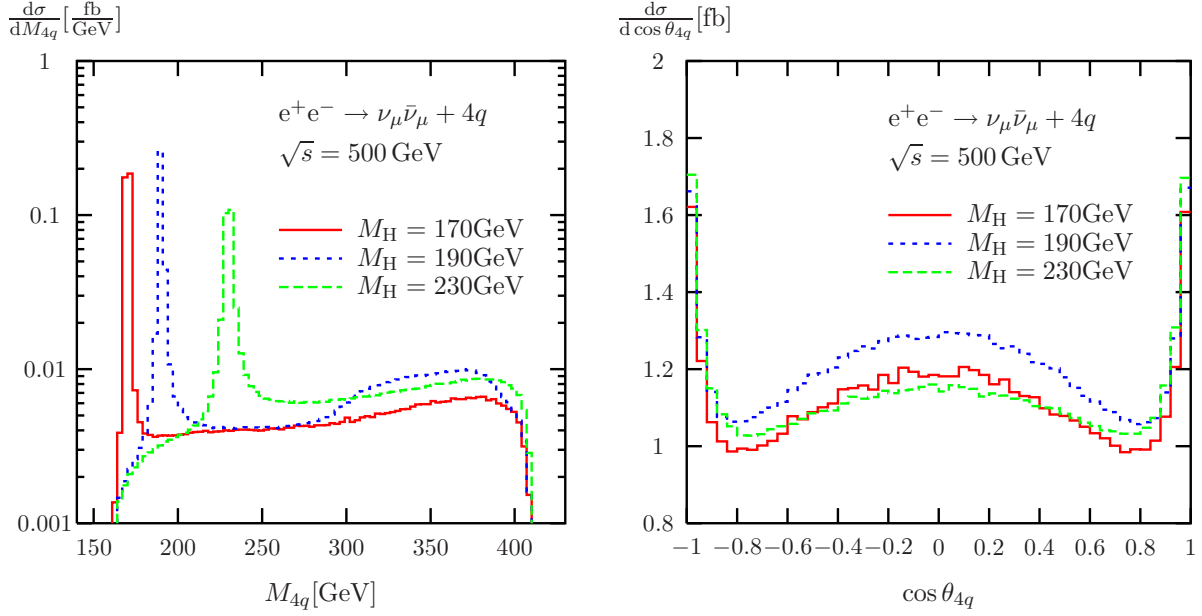


Figure 14: Invariant-mass and angular distributions of the four-quark system in $e^+e^- \rightarrow \nu_\mu \bar{\nu}_\mu + 4q$ (without ISR and gluon-exchange diagrams) for various Higgs masses and $\sqrt{s} = 500 \text{ GeV}$

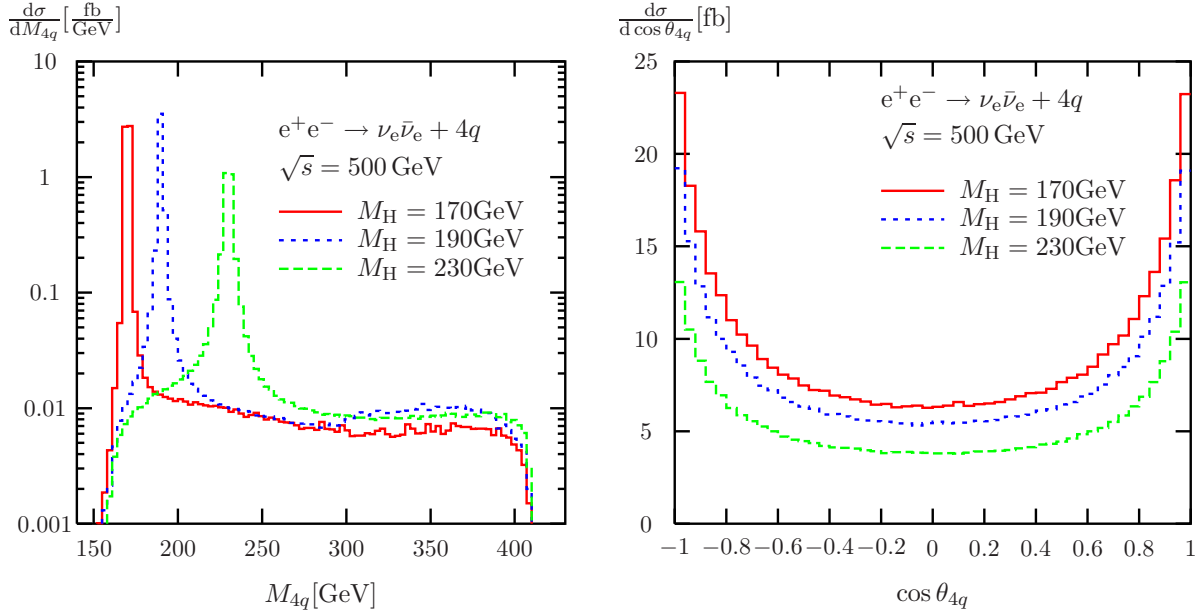


Figure 15: Invariant-mass and angular distributions of the four-quark system in $e^+e^- \rightarrow \nu_e \bar{\nu}_e + 4q$ (without ISR and gluon-exchange diagrams) for various Higgs masses and $\sqrt{s} = 500 \text{ GeV}$

the cross section of $\nu_e\bar{\nu}_e + 4q$ is an order of magnitude larger than the one of $\nu_\mu\bar{\nu}_\mu + 4q$. The invariant-mass distributions of the two channels look similar, and for $M_H = 170$ GeV resemble the shape already observed for the single channel $e^+e^- \rightarrow \nu_\mu\bar{\nu}_\mu u\bar{d}s\bar{c}$ in Figure 12. Note that for $M_H = 190$ GeV and 230 GeV the high-energy tails of the distributions show some Higgs mass dependence. This is due to the subprocess of ZH production where the Higgs decays via $H \rightarrow ZZ \rightarrow (\nu_\mu\bar{\nu}_\mu/\nu_e\bar{\nu}_e) + 2q$, which is not yet possible for the smaller Higgs mass $M_H = 170$ GeV. The corresponding boundary in M_{4q} , which is clearly seen in the plots for $M_H = 190$ GeV, is determined by the two extreme situations where the decay $H \rightarrow ZZ$ proceeds along the ZH production axis. For $M_H = 230$ GeV this boundary is hidden by the Higgs peak and the upper kinematical limit in the M_{4q} spectrum. In contrast to the invariant-mass distributions, the shape of the four-quark angular distributions of the $\nu_\mu\bar{\nu}_\mu$ and $\nu_e\bar{\nu}_e$ channels look very different. For $\nu_\mu\bar{\nu}_\mu$, i.e. for ZH production, intermediate production angles dominate, and this dominance is more pronounced for smaller Higgs-boson masses, where more phase space exists. For $\nu_e\bar{\nu}_e$, i.e. W-boson fusion, forward and backward production of Higgs bosons is preferred, and the M_H dependence is mainly visible in the overall scale of the distribution, but not in the shape itself.

6.5 Finite-width decay widths and gauge-invariance violation

We conclude our discussion of numerical results by considering the behaviour of various cross sections in the high-energy limit, using the different schemes for introducing finite decay widths as described in Section 2.3. Table 7 shows the results for the three reactions $e^+e^- \rightarrow \mu^-\bar{\nu}_\mu u\bar{d}b\bar{b}$, $e^+e^- \rightarrow \mu^-\bar{\nu}_\mu + 4q$, and $e^+e^- \rightarrow \nu_e\bar{\nu}_e\mu^-\bar{\nu}_\mu u\bar{d}$, which are typical representatives for top-quark pair production, WWZ production, and $WW \rightarrow WW$ scattering. All three examples confirm the expectation from $4f(+\gamma)$ studies that the fixed-width scheme, in spite of violating gauge invariance, practically yields the same results as the complex-mass scheme that maintains gauge invariance. For the first two processes the step width and the fixed width lead to the same results, since no propagators of unstable particles with space-like momenta (t -channel propagators) contribute, i.e. the widths in the propagators are never switched off by the step function in Eq. (2.48). For the last example, the difference between fixed and step widths is also marginal. In this context, the comparison with the WHIZARD and MADGRAPH results is particularly interesting, since MADGRAPH employs the step width within the unitary gauge, in contrast to LUSIFER, where the ‘t Hooft–Feynman gauge is used. Thus, there is a difference between the MADGRAPH and LUSIFER results for the step width, since gauge invariance is broken in this approach. However, this difference is not yet numerically significant in the shown numbers. Finally, all examples of Table 7 show that the running-width scheme breaks gauge invariance so badly that deviations from the complex-mass scheme are already visible below 1 TeV. Above 1 TeV these deviations grow rapidly, and the high-energy limit of the prediction is totally wrong.

From these results we can draw similar conclusions as known from $4f(+\gamma)$ production. If finite decay widths are introduced on cost of gauge invariance, the result is only reliable if it has been compared to a gauge-invariant calculation, as it is for instance provided by the complex-mass scheme. Moreover, our numerical studies show that the fixed-width scheme is in fact a good candidate for reliable results also in six-fermion production,

$\sigma(e^+e^- \rightarrow \mu^- \bar{\nu}_\mu u \bar{d} b \bar{b})$ [fb]						
\sqrt{s} [GeV]		500	800	1000	2000	10000
LUSIFER	fixed width / step width	17.095(11)	8.6795(83)	6.0263(76)	1.8631(31)	0.08783(28)
	running width	17.106(10)	8.6988(85)	6.0700(73)	2.3858(31)	212.61(28)
	complex mass	17.085(10)	8.6773(84)	6.0249(76)	1.8627(31)	0.08800(32)
W.&M.	step width	17.1025(80)	8.6823(44)	6.0183(31)	1.8657(12)	0.08837(20)

$\sigma(e^+e^- \rightarrow \mu^- \bar{\nu}_\mu + 4q)$ [fb]						
\sqrt{s} [GeV]		500	800	1000	2000	10000
LUSIFER	fixed width / step width	2.9603(28)	2.5949(26)	2.3573(25)	1.4055(20)	0.22593(63)
	running width	2.9845(25)	2.7354(25)	2.6829(27)	5.2921(66)	1623.0(30)
	complex mass	2.9600(25)	2.5948(26)	2.3559(25)	1.4048(20)	0.22532(63)
W.&M.	step width	2.9616(13)	2.5932(13)	2.3611(13)	1.4082(11)	0.2224(12)

$\sigma(e^+e^- \rightarrow \nu_e \bar{\nu}_e \mu^- \bar{\nu}_\mu u \bar{d})$ [fb]						
\sqrt{s} [GeV]		500	800	1000	2000	10000
LUSIFER	fixed width	1.6326(12)	4.1046(35)	5.6795(61)	11.736(16)	26.380(55)
	step width	1.6333(12)	4.1044(37)	5.6720(56)	11.734(15)	26.380(55)
	running width	1.6398(12)	4.1324(39)	5.7206(54)	12.881(14)	12965(12)
	complex mass	1.6330(12)	4.1037(34)	5.6705(54)	11.730(14)	26.387(57)
W.&M.	step width	1.6313(13)	4.1053(35)	5.6695(49)	11.741(12)	26.565(83)

Table 7: Born cross sections (without ISR and gluon-exchange diagrams) for $e^+e^- \rightarrow \mu^- \bar{\nu}_\mu u \bar{d} b \bar{b}$, $e^+e^- \rightarrow \mu^- \bar{\nu}_\mu + 4q$ and $e^+e^- \rightarrow \nu_e \bar{\nu}_e \mu^- \bar{\nu}_\mu u \bar{d}$ for various CM energies and schemes for introducing decay widths

although it does not respect gauge invariance. Whether this observation generalizes to all $6f$ final states (or even further) is, however, not clear.

7 Summary and outlook

The investigation of six-fermion production is one of the most important tasks at a future high-energy e^+e^- collider owing to a variety of interesting subprocesses leading to such final states. These, in particular, comprise top-quark pair production, massive vector-boson scattering, triple gauge-boson production, and Higgs-boson production for intermediate Higgs masses.

In this paper, the Monte Carlo event generator LUSIFER has been introduced, which in its first version deals with all processes $e^+e^- \rightarrow 6$ fermions at tree level in the Standard Model. In the predictions all Feynman diagrams are included, the number of which is typically of the order of 10^2 – 10^4 . Fermions other than top quarks, which are not allowed as external fermions, are taken to be massless, and polarization is fully supported. The helicity amplitudes are generically calculated with spinor methods and are presented explicitly. The phase-space integration is based on the multi-channel Monte Carlo integration technique. More precisely, channels and appropriate mappings are provided for each individual diagram in a generic way. Owing to the potentially large number of Feynman diagrams per final state, an efficient generic approach has been crucial, in order to gain an acceptable speed and stability of the program. Initial-state radiation is included at the leading logarithmic level employing the structure-function approach.

The performance of LUSIFER has been demonstrated in detail. In particular, a comprehensive survey of cross section results is presented, including all final states with up to three neutrinos and up to four quarks. Moreover, these cross sections are confronted with results obtained with the multi-purpose packages WHIZARD and MADGRAPH in a tuned comparison, as far as these programs were applicable. Apart from a few cases, where the limitations of WHIZARD and MADGRAPH becomes visible, we find good numerical agreement.

We have supplemented the numerical results on cross sections by presenting some distributions that are phenomenologically interesting for top-quark pair and Higgs-boson production. A comparison to WHIZARD and MADGRAPH results shows also in this case good agreement within statistical errors.

Finally, we have numerically investigated possible effects from gauge-invariance violation due to the introduction of the finite decay widths of unstable particles in the amplitudes. Similarly to the known results in four-fermion production, it turns out that the use of running decay widths in general leads to a totally wrong high-energy behaviour of the cross section, since gauge cancellations are disturbed. Although an approach based on fixed gauge-boson widths does not maintain gauge invariance either, the gauge-breaking effects are found to be sufficiently suppressed in the considered examples. This conclusion is based on a comparison with the gauge-invariant result obtained in the so-called complex-mass scheme, where gauge invariance is restored by introducing appropriate complex couplings that are derived from complex mass parameters.

Apart from emphasizing the issue of speed and stability, a third motivation in the construction of LUSIFER lies in the simplicity and flexibility of both the underlying concept

and the actual computer code. This simplicity considerably facilitates the task of going a step further in theoretical sophistication, i.e. beyond a tree-level Monte Carlo program improved by universal corrections. The high accuracy of future e^+e^- colliders requires the inclusion of non-universal radiative corrections to subprocesses such as top-quark pair and Higgs-boson production, or vector-boson scattering. To improve LUSIFER accordingly will be the subject of future work.

Acknowledgements

We thank Wolfgang Kilian for his aid in the WHIZARD installation and Tim Stelzer and David Rainwater for their help in the application of MADGRAPH to six-fermion production processes. Moreover, Ansgar Denner is gratefully acknowledged for discussions and for carefully reading the manuscript. This work was partially supported by the European Commission 5th framework contract HPRN-CT-2000-00149.

References

- [1] E. Accomando *et al.* [ECFA/DESY LC Physics Working Group Collaboration], Phys. Rept. **299** (1998) 1 [hep-ph/9705442];
J. A. Aguilar-Saavedra *et al.*, TESLA Technical Design Report Part III: Physics at an e^+e^- Linear Collider, hep-ph/0106315.
- [2] M. W. Grünewald *et al.*, in *Reports of the Working Groups on Precision Calculations for LEP2 Physics*, eds. S. Jadach, G. Passarino and R. Pittau (CERN 2000-009, Geneva, 2000), p. 1 [hep-ph/0005309].
- [3] F. Yuasa, Y. Kurihara and S. Kawabata, Phys. Lett. B **414** (1997) 178 [hep-ph/9706225].
- [4] T. Ishikawa, T. Kaneko, K. Kato, S. Kawabata, Y. Shimizu and H. Tanaka [MINAMI-TATEYA group Collaboration], KEK-92-19.
- [5] E. Accomando, A. Ballestrero and M. Pizzio, Nucl. Phys. B **512** (1998) 19 [hep-ph/9706201].
- [6] E. Accomando, A. Ballestrero and M. Pizzio, hep-ph/9709277.
- [7] F. Gangemi, G. Montagna, M. Moretti, O. Nicrosini and F. Piccinini, Nucl. Phys. B **559** (1999) 3 [hep-ph/9905271].
- [8] A. Ballestrero and E. Maina, Phys. Lett. B **350** (1995) 225 [hep-ph/9403244];
A. Ballestrero, hep-ph/9911318.
- [9] F. Caravaglios and M. Moretti, Phys. Lett. B **358** (1995) 332 [hep-ph/9507237].
- [10] K. Kolodziej, hep-ph/0110063.
- [11] F. Gangemi, hep-ph/0002142.

- [12] R. Chierici, S. Rosati and M. Kobel, LC-PHSM-2001-038, *2nd ECFA/DESY Study 1998–2001*, p. 1906.
- [13] M. Moretti, T. Ohl and J. Reuter, LC-TOOL-2001-040, *2nd ECFA/DESY Study 1998–2001*, p. 1981 [hep-ph/0102195].
- [14] W. Kilian, LC-TOOL-2001-039, *2nd ECFA/DESY Study 1998–2001*, p. 1924.
- [15] G. Montagna, M. Moretti, O. Nicrosini and F. Piccinini, Eur. Phys. J. C **2** (1998) 483 [hep-ph/9705333].
- [16] E. Accomando, A. Ballestrero and M. Pizzio, Nucl. Phys. B **547** (1999) 81 [hep-ph/9807515].
- [17] F. Gangemi, G. Montagna, M. Moretti, O. Nicrosini and F. Piccinini, Eur. Phys. J. C **9** (1999) 31 [hep-ph/9811437].
- [18] C. G. Papadopoulos, Comput. Phys. Commun. **137** (2001) 247 [hep-ph/0007335]; A. Kanaki and C. G. Papadopoulos, Comput. Phys. Commun. **132** (2000) 306 [hep-ph/0002082] and hep-ph/0012004.
- [19] S. Moretti, Phys. Lett. B **420** (1998) 367 [hep-ph/9711518], Nucl. Phys. B **544** (1999) 289 [hep-ph/9808430], and Eur. Phys. J. C **9** (1999) 229 [hep-ph/9901438].
- [20] F. A. Berends, R. Pittau and R. Kleiss, Nucl. Phys. B **424** (1994) 308 [hep-ph/9404313] and Comput. Phys. Commun. **85** (1995) 437 [hep-ph/9409326].
- [21] A. Denner, S. Dittmaier, M. Roth and D. Wackeroth, Nucl. Phys. B **560** (1999) 33 [hep-ph/9904472].
- [22] A. Denner, S. Dittmaier, M. Roth and D. Wackeroth, Phys. Lett. B **475** (2000) 127 [hep-ph/9912261]; Nucl. Phys. B **587** (2000) 67 [hep-ph/0006307]; Eur. Phys. J. C **20** (2001) 201 [hep-ph/0104057].
- [23] S. Dittmaier, Phys. Rev. D **59** (1999) 016007 [hep-ph/9805445].
- [24] F. A. Berends, P. H. Daverveldt and R. Kleiss, Nucl. Phys. B **253** (1985) 441; J. Hilgart, R. Kleiss and F. Le Diberder, Comput. Phys. Commun. **75** (1993) 191.
- [25] R. Kleiss and R. Pittau, Comput. Phys. Commun. **83** (1994) 141 [hep-ph/9405257].
- [26] E. A. Kuraev and V. S. Fadin, Yad. Fiz. **41** (1985) 753 [Sov. J. Nucl. Phys. **41** (1985) 466];
G. Altarelli and G. Martinelli, in *“Physics at LEP”*, eds. J. Ellis and R. Peccei, CERN 86-02 (CERN, Geneva, 1986), Vol. 1, p. 47;
O. Nicrosini and L. Trentadue, Phys. Lett. B **196** (1987) 551; Z. Phys. C **39** (1988) 479;
F. A. Berends, W. L. van Neerven and G. J. Burgers, Nucl. Phys. B **297** (1988) 429; Erratum-ibid. B **304** (1988) 921.

- [27] W. Beenakker *et al.*, in *Physics at LEP2*, eds. G. Altarelli, T. Sjöstrand and F. Zwirner (CERN 96-01, Geneva, 1996), Vol. 1, p. 79 [hep-ph/9602351].
- [28] T. Stelzer and W. F. Long, Comput. Phys. Commun. **81** (1994) 357 [hep-ph/9401258]; H. Murayama, I. Watanabe and K. Hagiwara, KEK-91-11.
- [29] M. Böhm, H. Spiesberger and W. Hollik, Fortsch. Phys. **34** (1986) 687;
A. Denner, Fortsch. Phys. **41** (1993) 307;
A. Denner, S. Dittmaier and G. Weiglein, Nucl. Phys. B **440** (1995) 95 [hep-ph/9410338].
- [30] R. G. Stuart, Phys. Lett. B **262** (1991) 113;
H. G. Veltman, Z. Phys. C **62** (1994) 35;
A. Aeppli, F. Cuyper and G. J. van Oldenborgh, Phys. Lett. B **314** (1993) 413 [hep-ph/9303236].
- [31] E. N. Argyres *et al.*, Phys. Lett. B **358** (1995) 339 [hep-ph/9507216];
W. Beenakker *et al.*, Nucl. Phys. B **500** (1997) 255 [hep-ph/9612260].
- [32] S. Dittmaier, hep-ph/9710542.
- [33] W. Beenakker, F. A. Berends and A. P. Chapovsky, Nucl. Phys. B **573** (2000) 503 [hep-ph/9909472].
- [34] T. Stelzer, private communications.
- [35] M. Roth, doctoral thesis, hep-ph/0008033.
- [36] E. Byckling and K. Kajantie, “*Particle Kinematics*” (Wiley, London, 1973) p. 158ff.
- [37] Y. Kurihara *et al.*, Prog. Theor. Phys. **103** (2000) 1199 [hep-ph/9912520] and Eur. Phys. J. C **20** (2001) 253 [hep-ph/0011276];
G. Montagna, M. Moretti, O. Nicrosini, A. Pallavicini and F. Piccinini, Eur. Phys. J. C **20** (2001) 217 [hep-ph/0005121];
G. Passarino, hep-ph/0101139 and Nucl. Phys. B **619** (2001) 313 [hep-ph/0108255].
- [38] D. E. Groom *et al.* [Particle Data Group Collaboration], Eur. Phys. J. C **15** (2000) 1.
- [39] A. Djouadi, J. Kalinowski and M. Spira, Comput. Phys. Commun. **108** (1998) 56 [hep-ph/9704448].
- [40] W. Kilian, private communications.